Electronic Research Archive

ERA, 32(4): 2541–2597.
DOI: 10.3934/era.2024117
Received: 09 December 2023
Revised: 05 February 2024
Accepted: 23 February 2024
Published: 28 March 2024

http://www.aimspress.com/journal/era

Research article

Minimally-intrusive, dual-band, fiber-optic sensing system for high-enthalpy exhaust plumes

Stephen A. Whitmore*, Cara I. Borealis and Max W. Francom

Department of Mechanical and Aerospace Engineering, Utah State University, 4130 Old Main Hill, Logan UT 44322, USA

* **Correspondence:** Email: Stephen.whitmore@usu.edu; Tel: +14357972951; Fax: +14357972417.

Abstract: The propulsion research lab at Utah State University has developed a minimally-intrusive optical sensing system for high-temperature/high-velocity gas-generator exhaust plumes. For this application glass fiber-optic cables, acting as radiation conduits, are inserted through the combustion chamber or nozzle wall and look directly into the flow core. The cable transmits data from the flame zone to externally-mounted spectrometers. In order to capture the full-optical spectrum, a blended dual-spectrum system was employed, with one spectrometer system tuned for best-response across the visible-light and near-infrared spectrum, and one spectrometer tuned for best-response in the near- and mid-infrared spectrum. The dual-band sensors are radiometrically-calibrated and the sensed-spectra are spliced together using an optimal Wiener filtering algorithm to perform the deconvolution. The merged spectrum is subsequently curve-fit to Planck's black-body radiation law, and flame temperature is calculated from associated curve maxima (Wien's law). The presented fiber-optic sensing systems performs a function that is analogous to Raman spectroscopy. The system non-contact, high-temperature measurement, and does not interfere with the heat transfer processes. In this report data collected from a lab-scale (200 N) hybrid rocket system are analyzed using the described method. Optically-sensed flame-temperatures are correlated to analytical predictions, and shown to generally agree within a few degrees. Additionally, local maxima in the optical spectra are shown to correspond to emission frequencies of atomic and molecular oxygen, water vapor, and molecular nitrogen; all species known to exist in the hybrid combustion plume. Presented data demonstrate that selected fiber-optics can survive temperature greater than 3000 ℃, for durations of up to 25 seconds.

Keywords: gas-generator; hybrid rocket; spectrometer; fiber-optic; black-body radiation; flame

temperature; dwell-time

Nomenclature:

A: *amplitude scaling factor*;
A_{burn}: *fuel port burn area,* cm^2;
A_{port}: *fuel port cross-sectional area,* cm^2;
A^*: *nozzle choking area,* cm^2;
a: *regression rate scale factor, cm/s*;
B: *black body spectral radiance,* $W/rad^2\text{-}m^3$;
c: *speed of light in a vacuum, 2.998 × 108 m/s*;
c^*: *characteristic velocity, m/s*;
D_{port}: *fuel port diameter,* cm;
F: *curve fit function,* $W/rad2\text{-}m^3$
$\partial F/\partial A$: *partial derivative of F with respect to A*;
$\partial F/\partial T$: *partial derivative of F with respect to T*;
F_{P_0}: *thrust calculated using chmber pressure and nozzle exit area, N*;
G_{ox}: *oxidizer massflux,* $g/cm^2\text{-}s$;
h: *Planck's constant, 6.62607015×10−34 J/Hz*;
i: *wavelength index*;
j: *iteration index*;
K: *QNEO spectrum scale factor*;
k_B: *Boltzmann constant, 1.380649×10−23 J/K*;
L: *fuel port length, cm*;
L^*: *combustion chamber characteristic-length, m*;
ΔM_f: *consumed fuel mass, g*;
$\dot{m}_{fuel}$: *fuel massflow, g/s*;
$\dot{m}_{ox}$: *oxidizer massflow, g/s*;
$\dot{m}_{exit}$: *nozzle exit or total massflow, g/s*;
n: *number of wavelengths, or fuel regression rate burn exponent*;
O/F: *oxidizer-to-fuel ratio*;
P_0: *combustion or stagnation pressure, kPa*;
R_g: *gas constant, J/kg-K*;
r_L: *longitudinal average of the fuel port radius, cm*;
r_0: *initial fuel port radius, cm*;
$\dot{r}_L$: *longitudinal mean of fuel regression rate, cm/s*;
S: *spectrum radiance at a single data point,* $W/rad^2\text{-}m^3$;
$\hat{S}$: *spectrum radiance adjusted for spectrometer response transfer function,* $W/rad^2\text{-}m^3$;
$\tilde{S}$: *filtered spectrum,* $W/rad^2\text{-}m^3$;
S/N_λ: *measured spectrum signal to noise ratio at given wavelength*;
S'_N : *signal-to-noise ratio intermediate value*;
T: *temperature, K*;

T_{flame}: *actual, or theoretical flame temperature K*;
$T_{optical}$: *optically-sensed flame measurement, k*;
T_0: *stagnation temperature, K*;
t_{burn}: *burn time, sec*;
V_{port}: *mean flow velocity in fuel port, m/s*;
ε: *numerical conditioning coefficient, W/rad*^{2}*-m*^{3}
η^* : *combustion efficiency*;
γ: *ratio of specific heats*;
Φ: *equivalence ratio*;
ρ_f: *solid fuel density, g/cm*^{3};
ρ_{ox}: *oxidizer flow density entering fuel port p, g/cm*^{3};
λ: *wavelength, nm*;
λ_{max}: *wavelength of maximum radiance, nm*;
τ_{dwell}: *combustor fuel port dwell time, s*;
Υ : *spectrometer response transfer function*;

1. Introduction

The project focuses on technologies for sensing flame and exhaust-gas temperature and compositional characteristics of high-temperature, high-velocity rocket and jet engine exhaust plumes. High-temperature, high-velocity, exhaust plumes present a uniquely challenging measurement environment. Wetted sensors, such as thermocouples and pressure transducers, degrade rapidly in reactive, particle-laden, high-temperature, and often highly-oxidizing plume flows. The hostility of this combustion environment presents a need for advanced, non-intrusive, non-immersion measurement techniques.

With the current state-of-the art, non-immersion measurements of gas-generator core-flows requires the installation of Gardon heat-flux gauges [1]. Gardon gauges are capable of sensing very high radiative heat flux levels, but require a complex and invasive installation. A typical installation must install the sensor into a port in the motor case sidewall, with a sapphire optical window protecting the gauge from the high temperatures. The Gardon gauge optical window is easily contaminated by the internal exhaust products, resulting in poor signal-to-noise ratio. The wall-mounted Gardon gauge is subjected to high acoustic and vibratory environments, and stress-fracture of the optical window is a frequent issue. For most installations, water cooling is required; thus, Gardon gauges cannot be used for fight applications. Thus, extending existing measurement technologies to operational systems requires improved strategies for reduced configuration intrusiveness, sensor survivability, and overcoming poor signal-to-noise ratio.

2. Background

The Propulsion Research Lab at Utah State University developed a novel, minimally-intrusive optical sensing system; whereby, glass fiber-optic cables, acting as radiation conduits, are inserted through the combustion chamber wall and look directly into the flow core. Although the fiber-optic cables inserted into the flow are consumed by the flame, the tips of the cables remain at the solid fuel boundary and recede at the same rate as the regressing fuel surface. As reported by Whitmore

et al. (2022) [2] and Whitmore et al. (2023) [3], preliminary hot-fire test results performed using a legacy lab-scale (200 N) hybrid rocket system burning gaseous oxygen (GOX) and Acrylonitrile-Butadiene-Styrene (ABS) as propellants. In this approach the glass fiber-optic cables, acting as radiation conduits, were inserted through the combustion chamber wall and look directly into the flow core. During the burn the fiber-optic cables were consumed by the flame, but remained flush to the fuel surface and continued to transmit light. These preliminary tests demonstrated that the inserted fiber-optics can survive temperature of up to 3000 ℃, for durations of up to 25 seconds. Data were gathered throughout the burn duration.

In the reported work the fiber-optic sensing technique was qualitatively successful in demonstrating feasibility. Unfortunately, for original feasibility assessment of Ref [2], as cost- and time-saving measures the tests employed "on-hand" duplex-mode fiber cable, originally designed for Infrared (IR) communications [4]. The duplex-cable passbands were across two distinct wavelengths, 1050 and 1300 nm. These passbands lie beyond of the optical range of the C11708MA spectrometer (640–1040 nm) [5] used for this assessment. Thus, the sensed spectra were highly attenuated, with emission line due to individual species smeared into the background black-body curve.

This deficiency was not discovered until after the completion of the initial feasibility assessments. Thus, the success of the early experiment was only partial, and the quantitative accuracy of the original optically-sensed temperature data remain unclear. In order to obtain quantitatively-accurate data, the overall objectives of the follow-on research to be reported here, is to improve the associated system calibration, extend the optical sensing range from the visible spectrum up through mid-infrared wavelengths, and develop more advanced analytical methods.

3. Theoretical considerations

This section details the theoretical and analytical methods that are essential to support the results of this study. A thermochemical analysis of the ABS fuel material and its combustion with gaseous oxygen is presented first. Analytical methods used to reduce and interpret the motor performance data will be presented next. Finally, the optimal filtering and curve-fitting methods used to interpret the plume spectra data and their correlations with the motor performance data will be presented.

3.1. Compositional analysis of the fuel material

The primary fuel used for this testing campaign was acrylonitrile butadiene styrene (ABS), a terpolymer material consisting of 1) acrylonitrile [6], 2) butadiene [7], and 3) styrene [8] monomers. For most commercially available industrial ABS preparations, the monomer mass fractions can vary widely, and, the precise chemical formulas including FDM feedstocks are tightly-held secrets. In order to reduce this uncertainty, Whitmore et al. [3] performed a series of Fourier Transform Infrared (FTIR) spectroscopy tests on several industrial ABS products in order to estimate the relative monomer proportions. Generally, as tested each of the products exhibited similar characteristics with mean mass proportions of approximately 1) acrylonitrile 28.4%, 2) butadiene 41.4%, and 3) styrene 30.5%. The corresponding chemical formula is $C_{4.399}\,H_{5.357}N_{0.337}$. The associated net-enthalpy of formation was calculated to be 60.11 kJ/g-mol. The values presented by Ref [3] are not proposed as set-numbers for each of the available industrial ABS preparations, but are presented only as typical values for industrial ABS preparations.

3.2. *Thermodynamic analysis of the combustion and nozzle exhaust plume*

The ABS total enthalpy and molecular weight estimates from Ref [3] were used to calculate the theoretical equilibrium combustion properties of ABS and gaseous oxygen, the propellants used for the hot-fire testing campaign to be described later in this paper. The thermo-chemical calculations were performed using the industry-standard NASA Chemical Equilibrium with Applications (CEA) tool [9]. These calculations assume 100% combustion efficiency η^*, and were performed with increasing oxidizer-to-fuel *O/F* ratios and combustion pressure levels. Figure 1 presents these results by plotting flame temperature T_0 and characteristic velocity c^*, calculated across a range of combustion (chamber) pressures P_0, varying 345 kPa (50 psia) to 5516 kPa (800 psia) in 170 kPa (25 psi) increments. Increasing values for T_0 and c^* are associated with increasing combustion pressures. The stoichiometric O/F ratio, approximately 2.29, is also plotted as the vertical dashed line. The red rectangle plotted on Figure 1 shows that the optimal O/F operating range for the propellants is very narrow, and moderately fuel-rich.

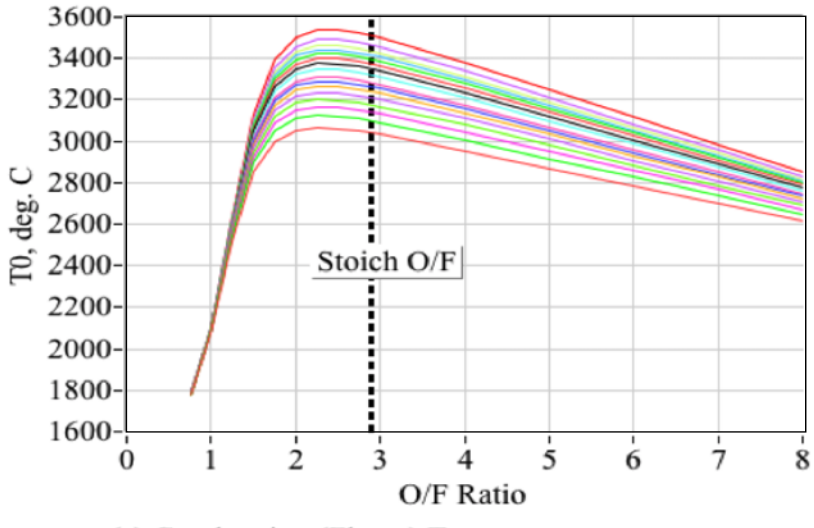

(a) Combustor Flame Temperature

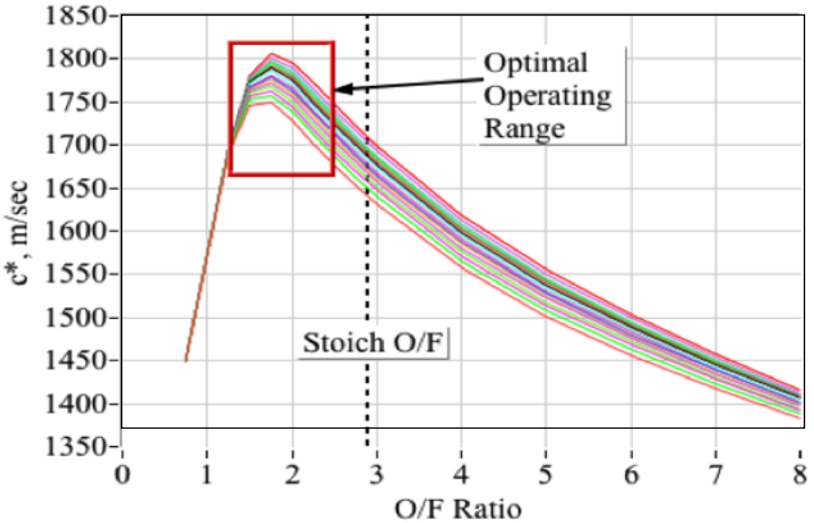

(b) Combustor Characteristic Velocity

Figure 1. CEA-derived flame temperate and characteristic velocity for GOX/ABS combustion.

The data of are Figure 1 used to estimate the nozzle exit gas temperatures. Assuming $\eta^* = 100\%$, Figure 2 shows this result for nozzle expansion ratios A_{exit}/A^* of 2.0, 4.0, 6.0, and 8.0. Note that the during adiabatic expansion through the nozzle, the maximum gas temperature drops from a range of 3050–3550 °C at the combustor, to a range of 2000–2150 °C at the nozzle exit for the expansion ratio of 8.0. For clarity Figures 4 and 5, only plot a limited number of combustor pressures varying from 145 (1000 kPa) to 870 psia (600 kPa).

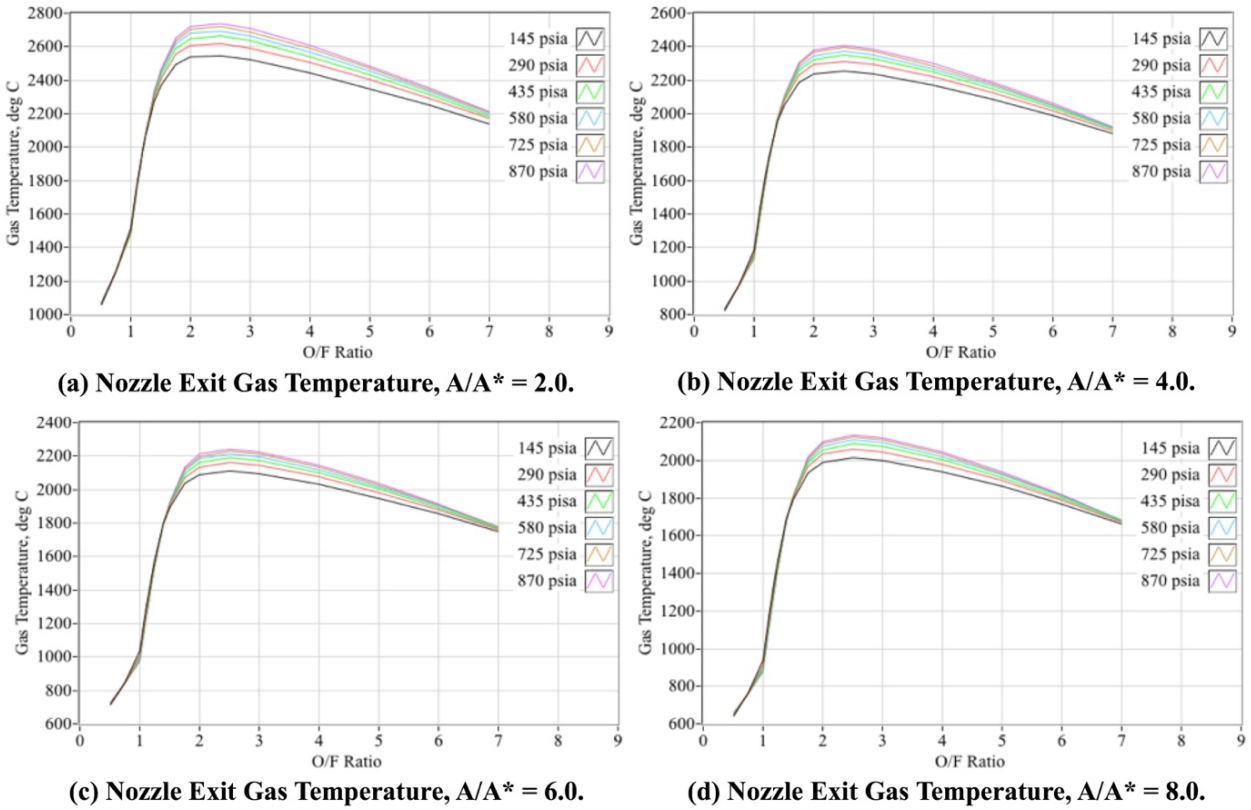

(a) Nozzle Exit Gas Temperature, A/A* = 2.0. **(b) Nozzle Exit Gas Temperature, A/A* = 4.0.**

(c) Nozzle Exit Gas Temperature, A/A* = 6.0. **(d) Nozzle Exit Gas Temperature, A/A* = 8.0.**

Figure 2. Theoretical GOX/ABS nozzle exit temperatures at $\eta^* = 100\%$.

3.3. Planck's Law relationship to black-body flame temperature

Planck's Law [10] describes the spectral density of electromagnetic radiation emitted by a black-body at a given temperature T, in thermal equilibrium with the surrounding environment,

$$B_A\left(\lambda,T\right)=2\cdot A\cdot\frac{h\cdot c^2}{\lambda^5}\cdot\frac{1}{e^{\left(\frac{h\cdot c\cdot}{\lambda\cdot k_B\cdot T}\right)}-1}. \tag{1}$$

In Eq (1) h is Planck's constant, c is the speed of light in a vacuum, k_B is Boltzmann's constant, λ is the emission wavelength, T is the absolute gas temperature, and A is the amplitude scaling factor. From Wien's displacement law [11], the optical wavelength λ_{max} associated with the maximum intensity given by Eq (1) is shown by Eq (2).

$$T_{flame} = \frac{2.8978 \times 10^{6}{}_{nm-K}}{\lambda_{\max}} \quad . \tag{2}$$

Because Eqs (1) and (2) demonstrate the relationship between the actual combustion/exit flame/plume temperatures of the rocket motor and the resulting spectrum, they are relevant to the current discussion.

Figure 3 plots λ_{max} for both the combustion chamber and nozzle exit temperatures as a function of O/F and the 4 expansion ratios of Figure 2.

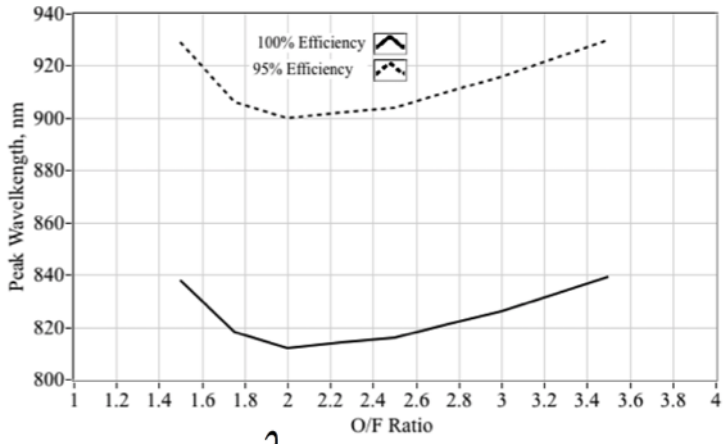

(a) Wiens Law $\lambda_{\max}$ for Combuston Chamber

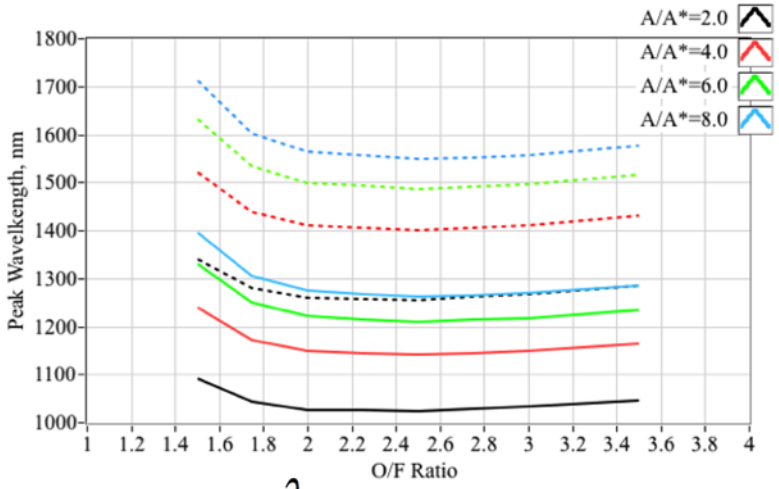

(b) Wiens Law $\lambda_{\max}$ for Nozzle Exit

Figure 3. Black-body peak-wavelengths in combustion chamber and nozzle.

The solid lines represent calculations assuming combustion efficiency η^* = 100%, and dashed lines represent calculations assuming η^* = 95%, where,

$$T_{actual} = \left(\eta^*\right)^2 \cdot T_{\substack{flame \\ theory}} \quad . \tag{3}$$

Note that near the optimal operating point, the shapes of the black-body curves for both the combustor and the nozzle exit, are not significantly affected by O/F, with only a slight redshift of the curve to the right at the lowest O/F ratios. In fact, even with this wide range of possible combustion temperatures, for the combustion chamber the corresponding peak amplitude wave lengths only range from 756 to 864 nm at 100% efficiency, and from 838 to 957 nm fat 95% efficiency. This range is relatively small with a mean value of approximately 895 nm, with a standard deviation of approximately 85 nm.

However, also note that the gas cooling associated with expansion through the nozzle has very significant effect, shifting blackbody peak-wavelength curve shifting the curve to the right, with the highest expansion ratios having peak-wavelengths well into the near IR-spectrum. here depending upon the expansion ratio and combustion efficiency, the black-body peak wavelengths can vary from 1000 nm to greater than 1600 nm.

3.4. Desired spectral range for fiber-optic sensing system

Thus, in order to properly characterize the full spectrum associated with hybrid rocket combustion, an appropriately "tuned" optical system must accurately characterize the spectrum response over a range from at least 400–1700 nm. As shown by Figure 4, this wavelength range requires sensing across the entire visible-light spectrum and also well-into the IR-A and IR-B portions of the near-infrared spectrum.

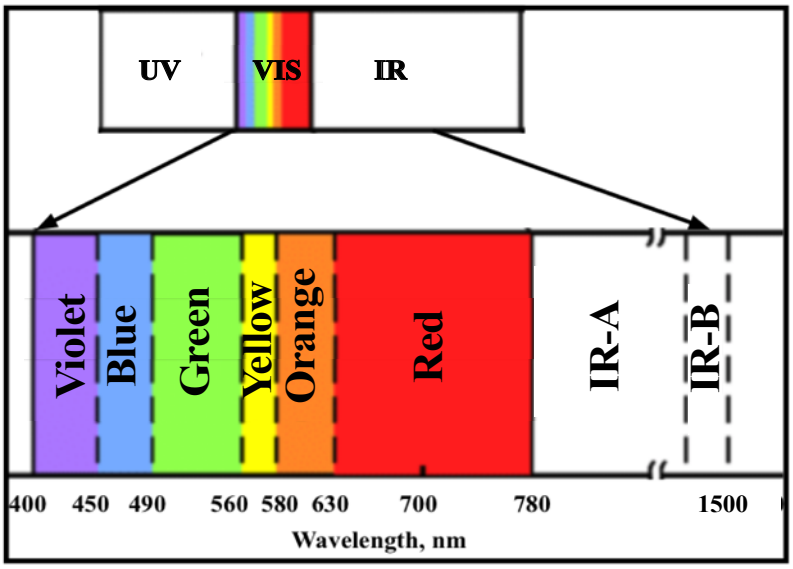

Figure 4. Visible and near-infrared spectrum.

Due to the wide required measurement range, and the different sensing elements necessary for obtaining visible-light and IR-B measurements, this analysis suggests that two individual spectrometers are required. In order to enhance the original sensing system capabilities, the proposed configuration uses one spectrometer designed for visible-light wavelengths, and one spectrometer designed for near-IR wavelengths. Details of this "dual-band" optical-systems design will be presented later in the Section 4 of the paper.

3.5. *Species concentrations bar graphs*

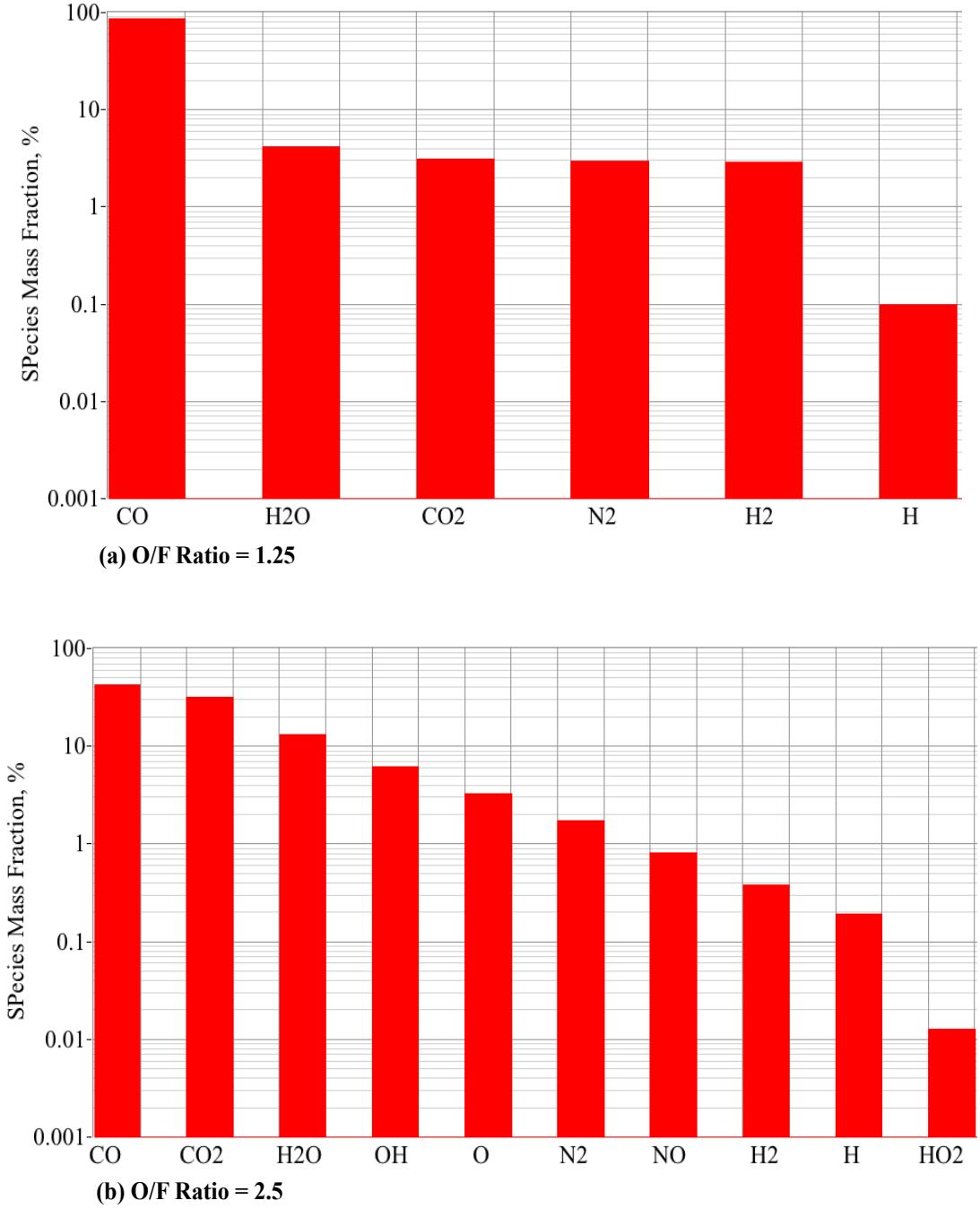

Figure 5. Theoretical GOX/ABS plume exhaust species for two o/f ratios.

The CEA code [9] also calculates the plume species concentrations for the various O/F ratios and pressure levels. Figure 5 shows example bar graphs that compares the combustion chamber species concentrations for two O/F ratios that span the designated optimal performance range of O/F = 1.25 and O/F = 2.5. The associated pressure level is 690 kPa (100psia) represents a median the operating chamber pressure for the hot-fire data to be presented later in this report. Across this optimal operating range the species concentrations vary significantly. At the richer O/F = 1.25 ratio, the predominant

species are carbon monoxide, water vapor, carbon-dioxide molecular nitrogen, and molecular hydrogen. For the leaner combustion products at O/F = 2.25, the predominant species are carbon monoxide CO, carbon dioxide CO_2, water vapor H_2O, hydroxyl OH, atomic oxygen O, and molecular nitrogen N_2. Trace amounts of nitric oxide NO, molecular H_2, and atomic hydrogen H, are also present. For the richer combustion products at O/F = 1.25, the associated species are CO, H_2O, CO_2, N_2, H_2, and H. For very fuel-rich combustion condensed carbon C (soot) are also predicted to be present.

Table 1 shows the predominant vacuum, neutrally-charged emission wavelengths associated with each of these species [12–19]. As shown by Table 1, the emission wavelengths of two dominant species, carbon monoxide, carbon dioxide lie well into the far-infrared range and are very difficult to sense using conventional spectroscopy. Spectral emission lines for oxygen, hydrogen, and nitrogen lie well within the visible wavelength range, and at the concentrations predicted by Figure 3, these plume species should be should be easily detectable. The absorption lines for water vapor lie outside of the visible range, but one wavelength at 1380 nm, should be detectable in the near-infrared spectrum range. Emission lines for carbon at 530, 687, and 904 nm should also be detectable when carbon is present for burns that are extremely fuel rich.

Table 1. Vacuum emission wavelength associated with known GOX/ABS exhaust plume species.

Species	Emission Wavelengths, nm
CO	1568, 2330, 4610
H_2	410, 434, 486, 656
H_2O	1380, 1870, 2700
H	364.6, 397, 410, 434, 486, 656
CO_2	300, 444, 1459
N_2	570, 670, 744, 746, 820, 870, 900, 970
OH	304, 307
O	558, 630, 635
C (Soot)	530, 687, 904

4. Materials and methods

This section describes the systems hardware used to perform the hot-fire testing campaign, and the analytical methods used to reduce and interpret the collected data. First, the legacy hybrid thrust chamber and support systems are described. Next, the required modifications and associated hardware necessary to better-optimize the fiber-optic system performance will be presented. The hardware, systems, and procedures necessary to calibrate the installed fiber optic systems will also be described. Finally, the analytical methods used to reduce the collected data will be presented. Only the final applications of the analytical methods will be presented in this section. Derivations of the analytical methods will be deferred to the original references, or to the appendices to this document.

4.1. Hybrid motor test systems

In this subsection a description of the hybrid motor thrust chamber will be presented first. A top-level description of the motor hot-fire support systems including ignition, fire control, and data

acquisition will follow. Detailed descriptions of the motor systems will be deferred to references.

4.1.1. Legacy 75-mm thrust chamber

Figure 6 shows the hybrid test motor as adapted for this testing campaign. Table 2 shows the top-level motor parameters. Major system components are: 1) the nozzle assembly, 2) nozzle retention ring, 3) motor case, 4) 3D printed ABS ignitor cap with embedded electrodes, extruded main fuel grain section, 5) insulating phenolic liner, 6) chamber pressure fitting, and 7) motor cap with a single-port injector. The 75-mm diameter motor case, constructed from 6061-T6 aluminum, was procured commercially [20].

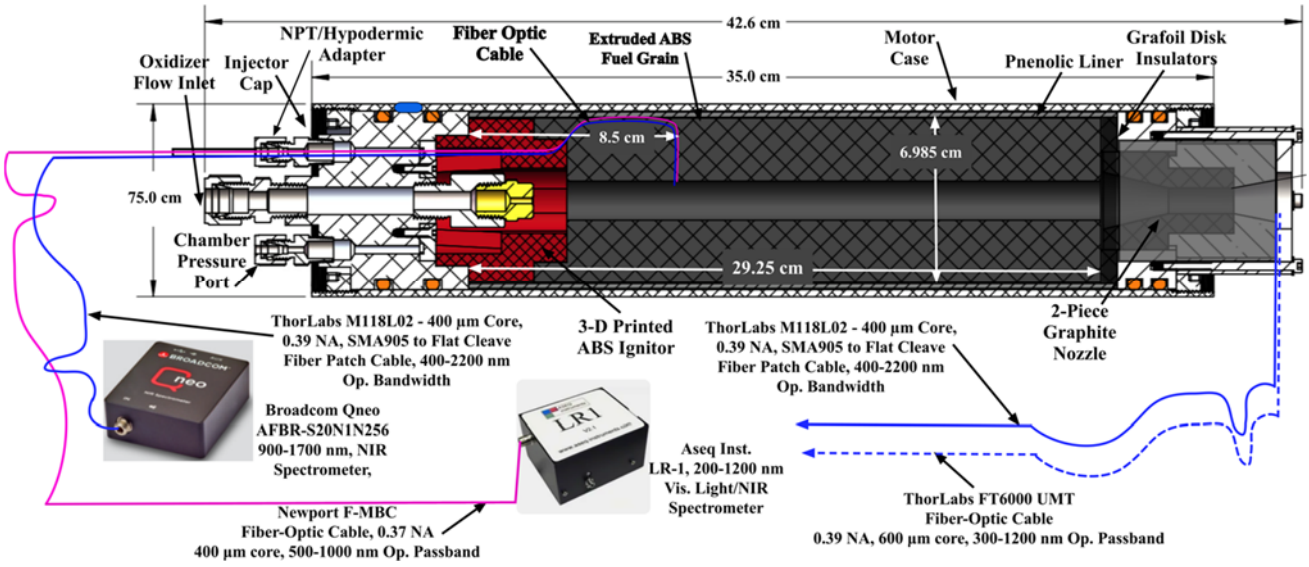

Figure 6. Legacy 75 mm hybrid motor adapted for fiber-optic measurement tests.

Table 2. 75-mm motor design parameters.

Component	Parameters
Performance	200 N Thrust (Nominal), 150 pisg Chamber Pressure, Exit Massflow 80 g/sec, Maximum Burn Lifetime 25 seconds
Injector	Single Port, Brass, 0.235 cm diameter, Cd = 0.95, Injector Feed Pressure 4140 kPa (500 psia)
Nozzle	One Piece Graphite, D^* = 1.25 cm, D_{exit} = 1.875 cm, A_e/A^* = 2.25, 10° Exit Cone
Fuel Grain	ABS, 29.25 cm total Length, 1.25 cm Initial Port Diameter, 6.35 cm outer fuel diameter, Density = 1.027/g.cm^3, Wght. = 360 grams
Oxidizer	GOX, Wght. = 1125 grams for 25 seconds burn

Figure 6 also shows the visible-light and IR-spectrometers and the associated fiber-optic cables

used to sense the internal and nozzle exit flame spectra. The fiber-optics are fed into the thrust chamber using an NPT-threaded hypodermic adapter, sealed against chamber pressure using high temperature silicone-adhesive. The nozzle exit plane was clamped n place using an aluminum ring attached to the nozzle retainer. The details of the optical-sensing hardware will be described later in this section.

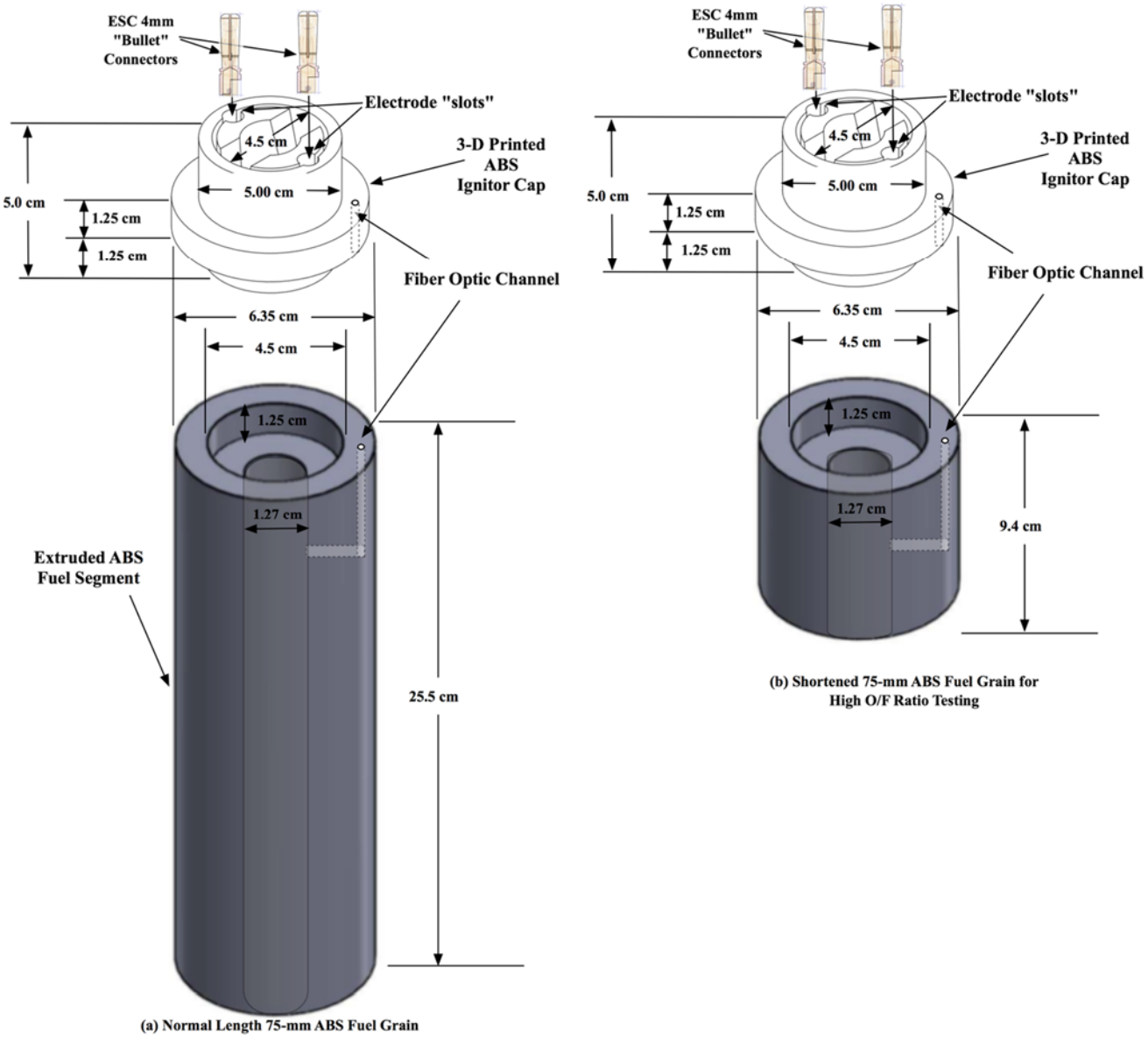

Figure 7. Comparing the full-length and shortened extruded abs fuel grain segments.

The acylonitrile butadiene styrene (ABS) fuel grain was fabricated in 2 pieces. The head-end section, depicted as the red segment was 3-D printed with channels allowing the fiber-optic cable to be routed through the injector cap, along the outer fuel grain wall and into the fuel port, and along the nozzle wall and into the fuel grain. The lower section of the fuel grain, pictured in grey, was machined from a solid piece of extruded ABS machined from a solid piece of extruded ABS, procured commercially [21]. For the lower section, the fiber-optic channel was machined into the fuel material. This design allows optical plume sensing at two points along the fuel port. A typical burn lift-time for the legacy motor was approximately 25 seconds.

In order to allow for significantly higher O/F ratios during the optical-systems testing, a significantly shorter fuel grain was specially developed for this testing campaign. Figure 7 compares the normal-length and shortened fuel grains. In the normal length-fuel the extruded grain segment is 25.5 cm in length; whereas, for the shortened grain, the extruded segment is only 10 cm in length. The 3-D printed ignitor segment is identical for both grain designs. The shortened grain is held into place by inserting a 15.5 cm aluminum spacer into the head end of the motor, above the injector cap. The spacer, injector cap, and fuel grain are held into place by the threaded locking ring. This modification allows for a significantly-leaner burn, with O/F ratios as high as 4 being achieved. This range of O/F ratios is critical for evaluating the effectiveness of the optical measurement systems across a range of flame temperatures.

The legacy hybrid rocket system features a patented [22] non-pyrotechnic, arc-ignition system developed at Utah State University. This low-wattage ignition system is enabled by recent advances in 3-D printing where additive manufacturing changes the electrical breakdown properties of the printed fuel. When the printed ABS segment is presented with a sufficiently high, electrical potential, arcing along the layered surface pyrolizes material and seeds combustion when an oxidizing flow is introduced. The ignition system power processing unit is based on the UltraVolt® line of high-voltage power supplies (HVPS) [23]. The HVPS provides a current-limited (60 mA) high voltage output of up to 500 V or 30 Watts total output. Ignition power to the thruster is initiated by sending a TTL-level activate logic bit to the HVPS.

4.1.2. Motor test support and measurement systems

Figure 8 shows the piping and instrumentation diagram (P&ID) of the motor test support and instrumentation systems. The motor is mounted to a calibrated thrust-stand with flexible mounts that allowed thrust transmission in the axial direction. Custom fire control, data acquisition, and processing software were pre-programmed to ensure run-to-run test consistency. Connection from the motor instrumentation pallet to the control/data logging laptop was via a single universal serial bus (USB). Test stand measurements include Venturi and flow-orifice based oxidizer mass flow rate, load-cell based thrust, chamber pressure, Oxidizer tank pressure, injector feed pressure, digital valve inlet and outlet pressures, and multiple thermocouples mounted at various points along the flow path. By assuming low stagnation pressure losses across the thrust chamber, a static pressure port/sensor installed at the nozzle allows the exit Mach number to be estimated.

The presented experimental apparatus used for this campaign has capability deep throttle using either an analog Ball Valve [24] or a patent-pending digital-valve throttle system. A hand-operated 3-Way valves selects between analog and digital control. The USU-developed digital throttle system, allow the test motor to be precision throttled over a range varying from 100% to less than 5% of design thrust level, with little effect on combustion-stability. The operational details of the digital throttle systems are currently restricted by the US Government as Controlled Unclassified Information (CIU), and cannot be released at this time. For the hot-fire testing campaign the throttle system is used to "tune" the motor response to achieve a wider range of O/F ratios.

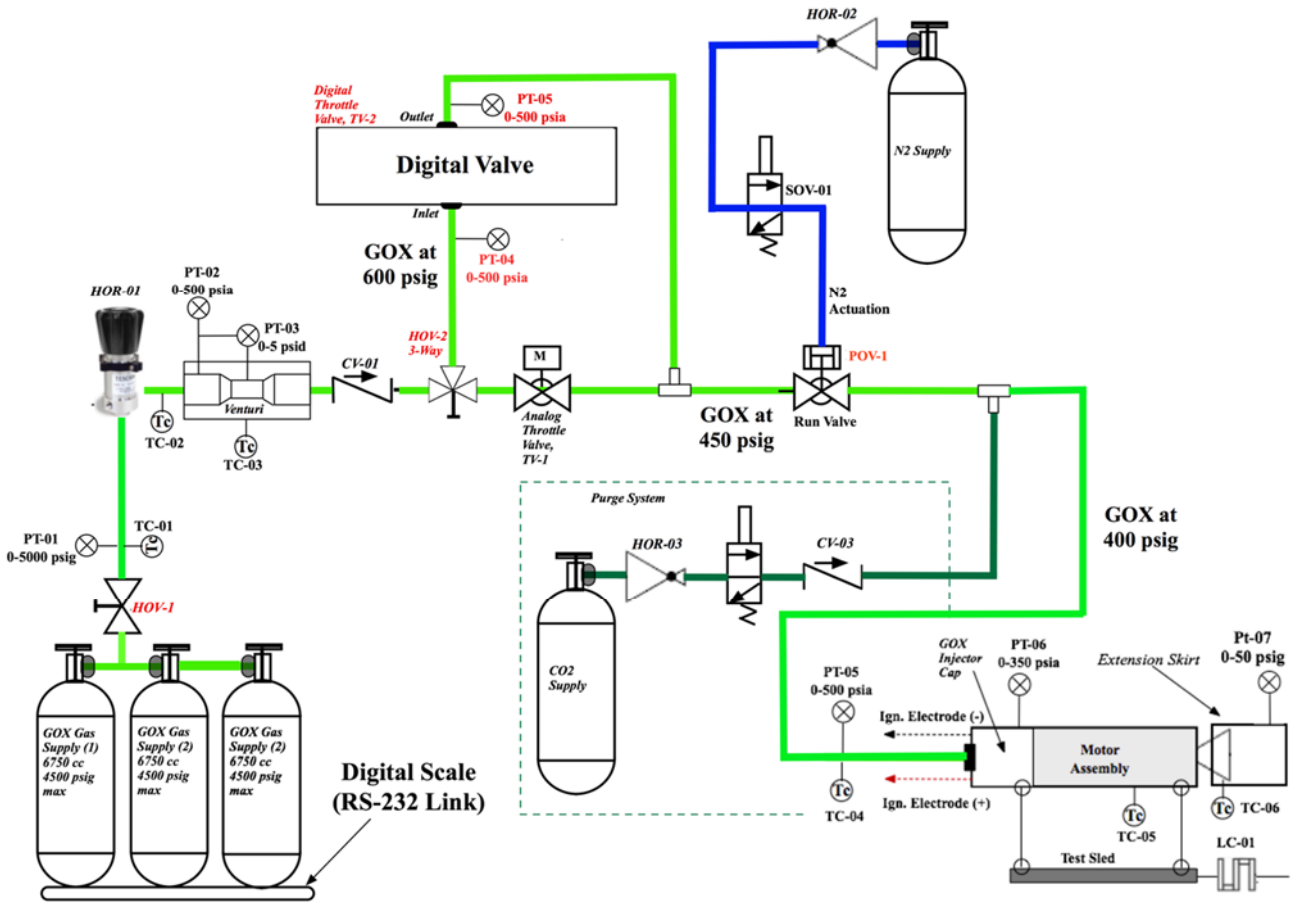

Figure 8. Test support systems piping & instrumentation (P&ID) diagram.

4.2. Spectrometer, fiber-optic instrumentation, and optical test support systems

The following sections describe the hardware improvements that were performed, upgrading the fidelity and accuracy of the sensing systems. The requirements for and the characteristics-of the selected spectrometers will be described first. Next the requirements for and the characteristics-of the associated fiber-optic cables will be presented. Finally, the calibration systems, procedures, and "best-practices" necessary to accurately calibrate the installed, end-to-end optical systems will be described.

4.2.1. Spectrometer selection

This section details the characteristics of the spectrometers selected for the follow-on hot-fire testing campaign. As per the earlier discussion of Section 3.4, both visible-light and near-IR spectrometers were evaluated. In order to capture the full-optical spectrum, a blended dual-spectrum system was eventually developed and employed. For this configuration, one spectrometer system was tuned for best-response across the visible-light and near-infrared spectrum, and one spectrometer was tuned for best-response in the near- and mid-infrared spectrum.

Hamamatsu C11708MA visible-light spectrometer

For this testing campaign, the original Hamamatsu C11708MA (Ref [5]) spectrometer as used for the feasibility assessment was replaced in favor of an alternative Hamamatsu C13985 miniature

spectrometer [25]. with a ready-made, industry-standard, SMA 905 [26] fiber-optic connector. The SMA 905 connector made swapping out and repairing damaged cables significantly easier during the preliminary-evaluation phase of this project. The C13985 spectrometer has a bandwidth range from 340 to 850 nm. Figure 9 shows the C1395 Spectrometer with the integral SMA 905 adapter, and the Universal Serial Bus (USB) interface to the acquisition computer.

Although the C13985 spectrometer generally behaved as designed, open-source software does not exist and the interface is made using a custom program provided by the manufacturer. Interfacing this custom-program with the existing Propulsion Research Lab (PRL) instrumentation system proved to be quite difficult. One of the key limitations was the inability to sufficiently "dial-down" the optical grid integration or exposure time. Thus, the spectrometer would experience frequent saturation conditions when the motor was operated at full throttle.

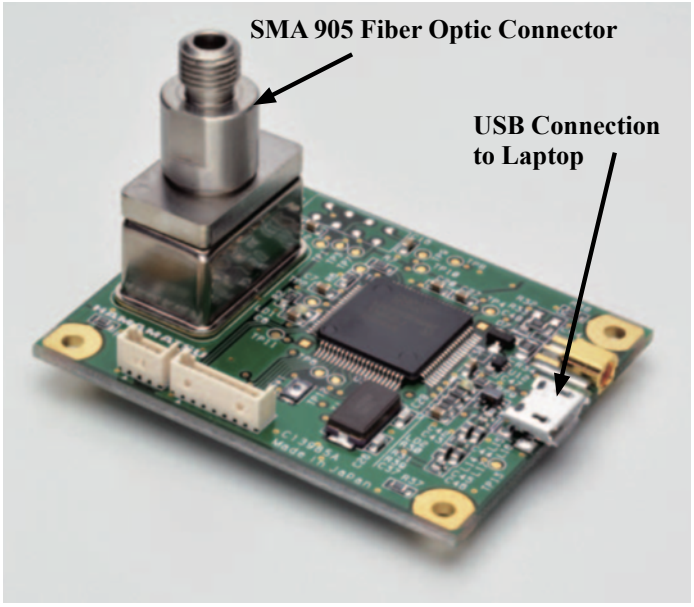

Figure 9. Hamamatsu C13985 visible-light spectrometer.

This saturation issue was mitigated by using in-line optical attenuators [27] that place a gap distance in the transmission line, decreasing the coupling efficiency. Gap Distances varying from 0.2 to 5.8 mm were used, sometimes in series, allowing different levels of attenuation to be achieved, depending upon the test conditions. Unfortunately, selecting the appropriate the in-line attenuators proved to be ad-hoc and very time consuming, resulting in the loss of significant amounts of test data. The C13985 spectrometer was eventually abandoned in favor of an alternative system using open-source software. However, some limited test results using the C13985 will be presented later in this report. Thus, a description of this spectrometer is included here for completeness.

ASEQ Instruments LR-1 visible-light spectrometer

The LR-1 miniature-Spectrometer [28], supplied by ASEQ Instruments would eventually replace the C13985 spectrometer. Figure 10 shows the LR-1 External case with the SMA-905 cable interface and USB Data Connection. The specified sensitivity range of the LR-1 is 200–1200 nm, although radiometric calibrations, whose data are to be resented later in the Section 5, showed that the bandwidth was significantly reduced, with the upper wavelength limit being around 900 nm. ASEQ Instruments

provided open-source software for the LR-1, and the sensor was easily interfaced with the existing PRL software and systems with a user-developed LabVIEW program. This interface program allowed to sensing grid exposure time to be easily controlled, allowing issues with optical saturation to be completely eliminated without the edition of optical attenuators. The LR-1 sampling rate is also easily controlled by the LabVIEW interface program. The mean sampling rate for the LR-1 was approximately 20 hertz, allowing up to 200 data frames to be collected during a 10-second burn.

Broadcom QNEO IR-spectrometer

As described in the Section 3.4 and also in the introduction to this section, for the "dual-band" system, a spectrometer tuned to sense in the near-infrared range is required to capture all of the hybrid plume blackbody spectrum salient features. For this test campaign the Broadcom QNEO [29] miniature IR-spectrometer was chosen. The QNEO, pictured in Figure 11, has a specified response range from 950–1700 nm, and is interfaced using custom-developed LabVIEW software. This open source interface allows the sensor grid exposure time to be easily controlled, avoiding the earlier-described sensor saturation issues. The QNEO package comes with an SMA 905 optical connector and a standard USB-C Laptop interface. The mean sampling rate for the QNEO was considerably slower than the LR-1, was approximately 1.5 hertz, allowing only 15 data frames to be collected during a 10-second burn.

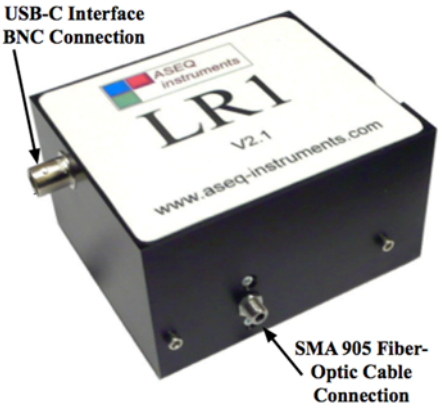

Figure 10. ASEQ instruments LR-1 visible light spectrometer.

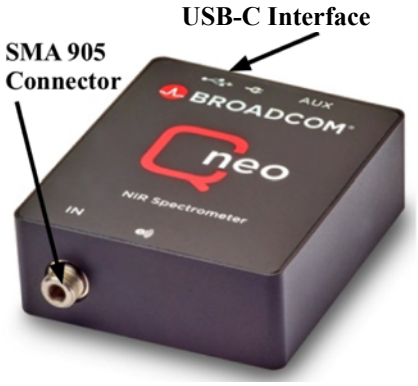

Figure 11. Broadcom QNEO IR spectrometer.

4.2.2. Fiber-optic cable selection

A typical optical fiber consists of a transparent core surrounded by an opaque or semi-opaque cladding. The core transmits an optical signal while the cladding guides the light within the core. The fiber-optic cable functions as a "wave guide," guiding the light introduced at one end of the cable through to the other end. The transmitted light stays confined to the core because the cladding has a lower refractive index than the core fiber.

Fiber-optic cables fall into three general classes [30], 1) single mode [31], 2) multi-mode [32], and 3) plastic optical fiber (POF) [33]. All of these fiber-classes were evaluated in this work before down-selecting to the best options. After some amount of trial-and-error three commercially-available fibers, tuned for either the visible-light or infrared spectra, were found to be acceptable for the detailed follow-on hot-fire testing campaign. Table 3 lists the top-level characteristics of these cables.

With the exception of the numerical aperture *NA*, the parameters are mostly self-explanatory. The numerical aperture, defined as the sine of the largest angle an incident ray total capture by the fiber core, is a measure of the acceptance angle of the fiber cable [34]. Because *NA* determines how well a fiber guides light, and allows resistance to bend-induced losses, it is an important consideration for this application. For the proposed plume-sensing application, the *NA* determines how diffuse the measurement becomes. A fiber-optic with a larger *NA* "scans" a wider region of the flow stream, whereas a small *NA* gives more of a pinpoint measurement. This selected *NA*'s are considered to be mid-range compromise values, allowing a well-defined "look" into the plume, without overly smearing the sensed results.

Table 3. Fiber-optic cables down-selected for detailed hot-fire testing campaign.

Cable Type	Part Number	Core Diameter	Transmission Wavelengths	Fiber NA	Color	Vendor
Multi-mode	Newport F-MBC [35]	400 μm	500–1100 nm (Visible/Near IR)	0.37	clear	www.newport.com
	Thor Labs FT600UMT [36]	600 μm	300–1200 nm (Visible/Near IR)	0.39	blue	www.thorlabs.com
	Thor Labs FT400EMT [37]	400 μm	400–2200 nm (Visible/Near IR)	0.39	blue with orange connector	www.thorlabs.com

As will be reported later in the results section, the "clear" Newport cable is the primary candidate for use in the combustion chamber at visible light and near-IR wavelengths using the Hamamatsu-13985 and LR-1 Spectrometers. Although this cable does not burn away as completely and smoothly as the POF cable, the resulting protrusion out from the fuel grain surface does not producing any visible distortions to the sensed spectrum. This cable is a bit fragile and needs to be handled with care when being installed into the motor fuel grain.

The “blue” Thor Labs cable is also well-suited for visible-light measurements using the Hamamatsu-13985 and LR-1 Spectrometers. Of all the cables tested during this campaign, this cable is by far the most resilient and is relatively difficult to damage or break. However, owing to the durability, this cable does not burn away as efficiency as does the “clear” Newport cable, and the protruding tip tends to get clogged with soot when used in the combustion chamber. For this research project, this cable was primarily used for external flow measurements, inserted into the nozzle exit plume. Details of the nozzle-exit plume exit measurements will be presented later in the Section 5 of this report.

Finally, the “blue and orange” Thor labs cable, due to its very wide transmission band, is primarily used for the IR (QNEO) spectrometer measurements. This cable burns away well, but is still quite durable, making it acceptable for both internal (combustor) and external (nozzle exit) applications. Conveniently, Thor labs provides pre-cut cable lengths with an SMA 905 a spectrometer adapter already attached, removing the need to install the adapter onto the upstream cable-end.

4.2.3. Installed fiber-optic configurations

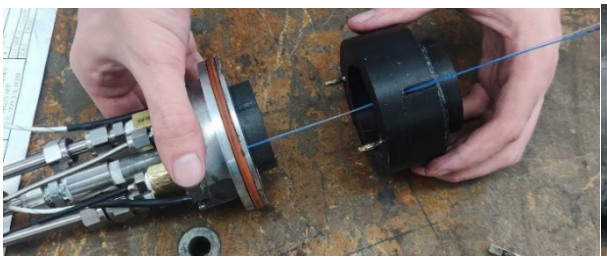

(a) Fiber-optic interface to injector/ ignitor caps

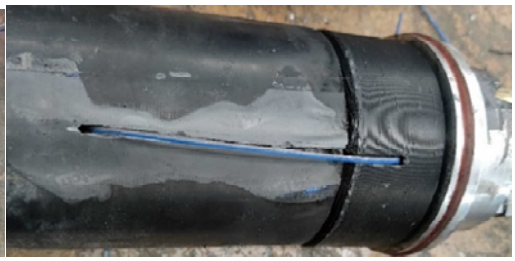

(b) Fiber-optic cable installed in fuel grain

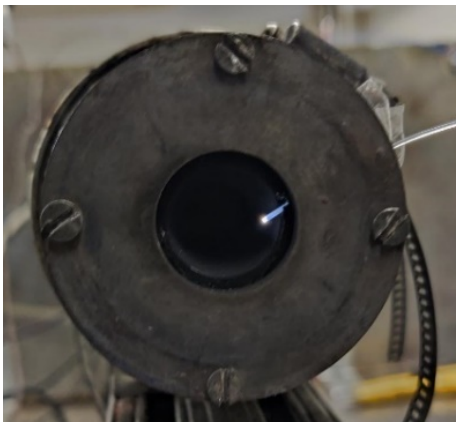

(c) Fiber-optic cable installed at nozzle exit plane

Figure 12. Fiber optic cable installation.

For this testing campaign one fiber-optic port was installed within the fuel grain, and one was installed at the nozzle exit plane. The combustion chamber fiber-optic was run into the fuel grain, through the injector cap hypodermic, through a 3-D printed port in the ignition cap, and into the combustion chamber using a channel cute along the outer edge of the fuel. At the sensing location, the fiber-optic was bent at the right angle and pointed to look directly into the center of the motor flame zone. Figure 12(a) shows the fiber optic interface the 3-D printed injector cap Figure 12(b) show the

installation of the fiber optic cables into the extruded fuel-grain segment. installation. The nozzle exit fiber-optic was installed externally to the motor case and was held in place by nozzle by an end plate. Figure 12(c) shows the nozzle exit plane installation. For best exit-plume visibility, the fiber-optic was positioned to protrude approximately one-third to one-half of the distance between the nozzle wall and the flame center, and the beginning of each burn. For this testing campaign the Thor Labs blue cable demonstrated the best durability and was used for the majority of the exit-plane tests.

4.2.4. Radiometric calibration equipment

In order to accurately derive the black-body spectrum from the sensed spectrometer data, it is essential that radiometric calibrations be performed on the "as installed" cable/ spectrometer configurations. The radiometric calibration [38] allows the sensitivity, or "transfer function" of the optical system to be measured as a function of input-light wavelength. The calibration also allows the accuracy of the output wavelength axis to be assessed and adjusted. Once measured, the transfer function is used to scale the raw spectrum amplitudes at each wavelength to account for the measurement system optical sensitivity. The adjusted spectrum represents the optical input, independent from the measurement system characteristics.

For this calibration a tungsten light-source, (part No. SLS201L) purchased commercially from Thor labs was used [39]. This high-accuracy high source presents a wide band spectrum, and approximates a black body source emitting at a temperature of 2796 K. Figure 13 compares the calibrated output from this light source against the corresponding black-body spectrum at 2796 K. Note that across the visible spectrum the light source closely matches the black body curve, but starts to drop away in the near IR-spectrum. This light source was carefully calibrated by the manufacturer to deliver a known spectrum of light with low-level of uncertainty. The tungsten light-source spectrum was measured using NIST traceable standards for traceability and reliability.

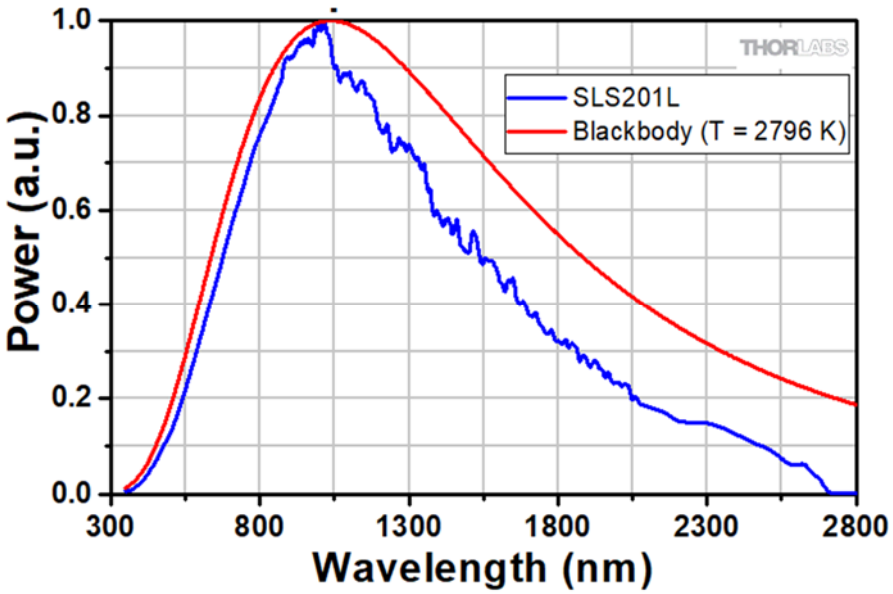

Figure 13. SLS201L tungsten light source calibration compared to black-body curve at 2796 K.

Figure 14 shows the calibration arrangement. Here the SLS201L tungsten light is connected to the spectrometer by the fiber-optic cable. For the C13985 and LR-1 spectrometers operating at visible-light wavelengths, the wavelength axis was also calibrated by using narrow-band optical filters with wavelengths centered at 450, 550, 650, 750, 850, and 1000 nm [40]. Each of the bandpass filters is conveniently designed to be inserted into the SLS201L tungsten lamp. The calibrations are repeated for each spectrometer/cable combination to derive the appropriate transfer function. For the infrared sensors, no IR pass-band filters are available and only the broad-band signal was used to perform the amplitude and wavelength axis calibration. Results of the radiometric calibration will be presented later in Section 5 of this paper.

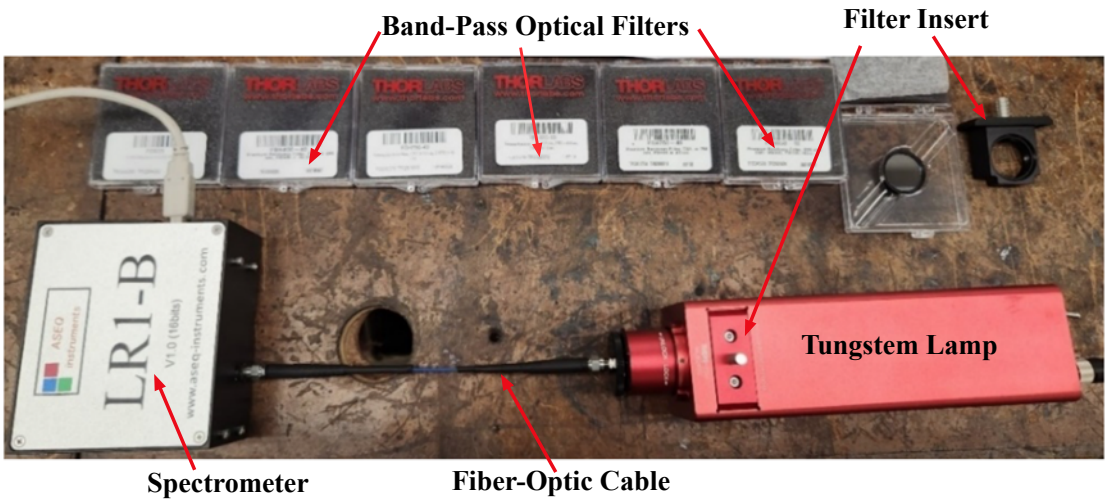

Figure 14. Apparatus for radiometric calibrations.

4.3. Analytical methods

This section presents the analytical methods used for reducing and interpreting the motor performance and spectrum data. Because the motor flame temperature is directly correlated to O/F ratio, the motor performance analysis, presented first, is essential interpreting the spectrum results. Next, the methods for processing the raw spectra in order to account for optical0systems end-to-end radiometric transfer function are presented. Finally, the curve analytical methods used fit the spectra, corrected for the radiometric transfer function, to Planck's Law are presented.

4.3.1. Estimating the instantaneous O/F ratio from performance data

As shown by the discussion of the previous section, the actual O/F ratio as achieved during hot-fire testing is a critical independent parameter for this testing campaign. As derived by Whitmore (2020) [41], the presented analysis is a summary of the methods for estimating the instantaneous O/F ratio during the burn. Due to the high levels of acoustical and vibration noise encountered during hot fire testing, it is extremely difficult to direct sense the rate of fuel consumption in real time. Thus, the rate of fuel consumption was indirectly inferred from a collection of other mechanical measurements. The analysis iteration begins with a calculation of the mean oxidizer-to-fuel ratio over the entire burn duration,

$$\bar{O}/\bar{F} = \frac{\int_{t_0}^{t_{burn}} \dot{m}_{ox}(t)\cdot dt}{\Delta M_f} \quad . \tag{4}$$

In Eq (4) the total consumed oxidizer mass is calculated using pre-and post-test total oxidizer tank mass from the oxidizer scale reading, as depicted by Figure 8. The total consumed fuel mass was measured by removing the thrust chamber from the test stand, post-test, weight the thrust chamber, and comparing to the pre-test thrust chamber weight.

Next, the nozzle exit massflow was calculated by the 1-dimensional De Laval choking mass flow equation, from Anderson [42, Chapt. 5], using the measured chamber pressure P_0, nozzle exit area A^*, and exhaust gas properties as inputs,

$$\dot{m}_{exit} = A^* P_0 \sqrt{\left(\frac{\gamma}{R_g \cdot T_0}\right)\left(\frac{2}{\gamma+1}\right)^{\frac{\gamma+1}{\gamma-1}}} \quad . \tag{5}$$

After calculating the total instantaneous massflow rate, the instantaneous fuel massflow rate is calculated as the difference between the measured oxidizer and nozzle exit mass flows according to Eq (6),

$$\dot{m}_f = \dot{m}_{exit} - \dot{m}_{ox} \quad . \tag{6}$$

The instantaneous oxidizer massflow rate of Eq (6) was calculated using the calibrated venturi flow meter as depicted by Figure 8. The venturi calculations were verified post-test by comparing the time-integrated oxidizer mass flow against consumer oxidizer massflow as measured by the oxidizer scale reading, also depicted by Figure 8.

In Eq (5) the thermodynamic parameters T_0, gas constant R_g, and ratio of specific heats γ, were calculated using 2-Dimensional table lookups of data generated using the CEA analysis of Figure 3 (Ref [9]), with chamber pressure (P_0), oxidizer-to-fuel ratio (O/F), and combustion efficiency (η^*) as independent variables. In this method η^* adjusts the actual flame temperature compared to the ideally expected value,

$$\eta^* = \frac{c^*_{actual}}{c^*_{ideal}} = \frac{\sqrt{\left(\frac{\gamma+1}{2\gamma}\right)^{\frac{\gamma+1}{\gamma-1}} \cdot R_g \cdot T_{0_{actual}}}}{\sqrt{\left(\frac{\gamma+1}{2\gamma}\right)^{\frac{\gamma+1}{\gamma-1}} \cdot R_g \cdot T_{0_{ideal}}}} \approx \sqrt{\frac{T_{0_{actual}}}{T_{0_{ideal}}}} \quad . \tag{7}$$

From Eq (5) the chamber pressure time history and instantaneous O/F ratio are used to calculate the total massflow for each time point. The O/F ratio is calculated as the instantaneous ratio of the oxidizer and fuel massflow rates, using Eqs (5) and (6). In this method, the value of η^* was iteratively

adjusted using a steepest-descent method, to produce a fuel mass flow rate whose integral over the burn duration matches the consumed fuel mass as measured after each test. Increasing the table lookup input value for η^* has the effect of decreasing the calculated fuel massflow rate, and decreasing η^* has the opposite effect. The iteration is initialized using the mean O/F ratio as calculated by Eq (4).

The total massflow of Eq (5) was verified by using the de-Laval flow equations to also calculate the predicted thrust levels, assuming negligible nozzle erosion, equations to write thrust in terms of the nozzle exit pressure ratio.

$$F_{P_0} = P_0 A^* \cdot \left(\sqrt{\frac{2}{\gamma - 1} \cdot \left(\frac{2}{\gamma + 1} \right)^{\frac{\gamma+1}{\gamma-1}} \left(1 - \frac{p_{exit}}{P_0} \right)^{\frac{\gamma-1}{\gamma}}} + \left(\frac{A_{exit}}{A^*} \right) \left(\frac{p_{exit} - p_\infty}{P_0} \right) \right). \tag{8}$$

In Eq (7) A_{exit} is the nozzle exit area, p_{exit} is the nozzle exit plane static pressure, and p_∞ is the local operating ambient pressure level. Given the thrust and massflow calculations of Eqs (6) and (7), other parameters of interest including specific impulse and characteristic velocity are easily calculated.

4.3.2. Signal-processing of the raw spectrum measurements

As described in the Section 4.3.1 In order to accurately derive the black-body spectrum, it is essential that transfer functions derived from radiometric calibrations be applied to the raw sensed-spectrum data. The optimal deconvolution algorithm as originally developed by Norbert Wiener in the frequency domain [43] is used for this analysis. The original method is modified to replace frequency with wavelength as the independent variable. Refs [2] and [3] develop this procedure. The deconvolution algorithm amplifies attenuated spectrum signals, while selectively rejecting sensor noise. The model inversion equation, as developed by Wiener, is presented by Eq (9),

$$\hat{S}(\lambda) = \left\{ \frac{\Upsilon(\lambda)\left(S / N_\lambda\right)^2}{\Upsilon(\lambda)^2 \left(S / N_\lambda\right)^2 + 1} \right\} S(\lambda), \tag{9}$$

$\hat{S}(\lambda)$ = adjusted spectrum, for input wavelength, λ

$S(\lambda)$ = raw input radiance at each λ

$\Upsilon(\lambda)$ = spectrometer transfer function coefficient @ λ

S / N_λ = signal-to-noise ratio at a given λ

.

The filter noise scaling parameter S/N_λ, technically represents the mean-square signal-to-noise ratio of the *unknown true input signal* but can be approximated by the square of the signal-to-noise ratio (S/N) of the *measured output signal*. The Wiener solution weights the spectrum coefficients to compensate for the S/N of the system as a function of the input signal wavelength. There are adaptive Wiener filtering algorithms that estimate S/N as part of the filtering process, but they are not applied here.

In this case, *S/N* values were chosen *a priori* based on the observed noise threshold of the raw

spectra signals. In order to estimate the S/N ratio the raw optical signal is first smoother using a finite-impulse response (FIR) filter [44]. The difference between the filtered and raw signals is used to approximate the random noise on the signal,

$$S \to Filtered,\ Smoothed\ T.F.\quad \tilde{S} \to Unfiltered\ T.F.\quad N \to \left|\tilde{S} - S\right|$$

Allowing for a numerical conditioning coefficient ε to avoid division by zero then,

$$S_N^{'} = \frac{S}{N+\varepsilon} = \frac{1}{\left(\frac{N}{S} + \frac{\varepsilon}{S}\right)}. \tag{10}$$

Solving for the signal-to-noise ratio at each wavelength,

$$\frac{S}{N}_{\lambda} = \frac{S}{\left(\frac{S}{S_N^{'}} - \varepsilon\right)}. \tag{11}$$

Because the signal-to-noise ratio appears in both the numerator and denominator of Eq (8), the absolute magnitude in not important. It is the variation of the S/N magnitude with respect to wavelength that provides the selective filtering of the Wiener filter. Thus, for this analysis the S/N estimates are normalized to give a peak magnitude of 1. Values of S/N, estimated from the measured data are presented later in the results, Section 5.2.

4.3.3. Fitting Planck's Law to the processed spectrum

Using the processed spectra, Equation (1) (Planck's law) is curve-fit to the data with the response amplitude A, and the temperature T, as independent variables. The presented algorithm is reasonably stable, as long as the initial guesses for $\{A, T\}$ are within approximately 30% of the "true" values. Using guidance from the CEA tables, an *ad hoc*, interactive procedure was developed used for picking these initial values. As developed by Refs [2] and [3], Planck's law is written as a function of T and A

$$F\left(A,T\right) \equiv B_A\left(\lambda,T\right) = 2 \cdot A \cdot \frac{h \cdot c^2}{\lambda^5} \cdot \frac{1}{e^{\left(\frac{h \cdot c \cdot}{\lambda \cdot k_B \cdot T}\right)} - 1}, \tag{12}$$

an iterative, non-linear least squares regression algorithm is applied. As derived by Refs [2] and [3] the iterative regression equation is,

$$\begin{bmatrix} A^{(j+1)} \\ T^{(j+1)} \end{bmatrix} = \begin{bmatrix} A^{(j)} \\ T^{(j)} \end{bmatrix} + \frac{\begin{bmatrix} \sum_{i=1}^{N}\left(\left\{\frac{\partial F}{\partial T}\right\}_{(i)}^{(j)}\right)^2 & -\sum_{i=1}^{n}\left(\left\{\frac{\partial F}{\partial A}\right\}_{(i)}^{(j)} \cdot \left\{\frac{\partial F}{\partial T}\right\}_{(i)}^{(j)}\right) \\ -\sum_{i=1}^{n}\left(\left\{\frac{\partial F}{\partial A}\right\}_{(i)}^{(j)} \cdot \left\{\frac{\partial F}{\partial T}\right\}_{(i)}^{(j)}\right) & \sum_{i=1}^{n}\left(\left\{\frac{\partial F}{\partial A}\right\}_{(i)}^{(j)}\right)^2 \end{bmatrix} \cdot \begin{bmatrix} \sum_{i=1}^{n}\left(\left\{\frac{\partial F}{\partial A}\right\}_{(i)}^{(j)} \cdot \left[S_{(i)} - F_{(i)}\left(A^{(j)}, T^{(j)}\right)\right]\right) \\ \sum_{i=1}^{n}\left(\left\{\frac{\partial F}{\partial A}T\right\}_{(i)}^{(j)} \cdot \left[S_{(i)} - F_{(i)}\left(A^{(j)}, T^{(j)}\right)\right]\right) \end{bmatrix}}{\sum_{i=1}^{N}\left(\left\{\frac{\partial F}{\partial A}\right\}_{(i)}^{(j)}\right)^2 \cdot \sum_{i=1}^{N}\left(\left\{\frac{\partial F}{\partial T}\right\}_{(i)}^{(j)}\right)^2 - \left(\sum_{i=1}^{n}\left(\left\{\frac{\partial F}{\partial A}\right\}_{(i)}^{(j)} \cdot \left\{\frac{\partial F}{\partial T}\right\}_{(i)}^{(j)}\right)\right)^2} \quad . \tag{13a}$$

In Eq (13) the symbol S represents the transfer function-adjusted spectrum, and for each parameter iteration j, the partial derivatives are calculated by,

$$\left\{\frac{\partial F}{\partial A}\right\} = 2 \cdot \frac{h \cdot c^2}{\lambda_{(i)}{}^5} \cdot \frac{1}{e^{\left(\frac{h \cdot c \cdot}{\lambda_{(i)} \cdot k_B \cdot T}\right)} - 1}, \tag{13b}$$

$$\left\{\frac{\partial F}{\partial T}\right\} = 2 \cdot A \cdot \left(\frac{h^2 \cdot c^3}{\lambda_{(i)}{}^6 \cdot k_B \cdot T^2}\right) \cdot \frac{e^{\left(\frac{h \cdot c \cdot}{\lambda_{(i)} \cdot k_B \cdot T}\right)}}{\left(e^{\left(\frac{h \cdot c \cdot}{\lambda_{(i)} \cdot k_B \cdot T}\right)} - 1\right)^2} \quad . \tag{13c}$$

For this black-body curve fitting procedure, any narrow-band emission or absorption spikes due to individual plume species are "notched-out" before performing the curve fit. Ref [44] described this notch-filtering procedure.

4.3.4. Optimally "splicing" the dual-band spectra together

For the dual-band sensing technique, in order to complete the entire Visible/IR spectrum, the deconvolved signals, adjusted for the radiometric functions using Eqs (8)–(10), must be "spliced" together. A factor making this splice challenging is the different output scales for the two spectrometers. For this process, the entire radiometrically-adjusted QNEO spectrum is multiplied by a wide range of scale factors, K. The scaled IR-data (QNEO) are then concatenated with the radiometrically-adjusted visible (LR-1) spectra,

$$\hat{S}(\lambda)=\left[\left\{\frac{\Upsilon(\lambda)\left(S/N_{\lambda}\right)^{2}}{\Upsilon(\lambda)^{2}\left(S/N_{\lambda}\right)^{2}+1}\right\}S(\lambda)\right]_{\substack{LR-1\\Visible}}+\mathrm{K}\cdot\left[\left\{\frac{\Upsilon(\lambda)\left(S/N_{\lambda}\right)^{2}}{\Upsilon(\lambda)^{2}\left(S/N_{\lambda}\right)^{2}+1}\right\}S(\lambda)\right]_{\substack{QNEO\\IR}} \tag{14}$$

and the combined data set is curve-fit using the methods of Eqs (12) and (13). The scale factor K that results in the minimum variance fit to Planck's law is selected. As will be shown in the results, Section 5.2, when the curve-fit variance is plotted against the range of scale-factors, the process is nearly quadratic, and the resulting minimum-variance value for K is near-optimal. "Best-practices" selecting the necessary range and densities of scale factors in order to give a near-optimal, minimum-variance solutions are presented in Section 5.2.

5. Results

This section presents the results of the testing campaign. Results from the radiometric calibration will be presented first. Next, several illustrative examples will be presented where the nozzle performance data are presented, and compared to the fiber-optic curve fitting results. Effects of the Wiener-filtering algorithm are illustrated, as well as "best-practices" for splicing the visible-light and IR-spectra to generate a broad-band spectrum that is curve fit using the methods of Eqs (10)–(13). Finally, a series of summary figures are presented illustrating the effectiveness, and expected accuracies of the sensing technique.

5.1. Radiometric calibration

As described in Sections 4.2.4 radiometric calibrations were performed for both the visible-light and IR spectrometers, and for three different cable-spectrometer combinations. This section described the results of these calibrations. The visible light calibrations are presented first, followed by the IR calibrations.

5.1.1. LR-1 visible light/near-IR calibrations

As previously described in Section 4.2, the primary visible-light configuration used for sensing the combustor spectra consisted of the Newport-clear fiber-optic cable, from Table 3, coupled to the LR-1 spectrometer. Figure 15 shows the composite calibration results. Plotted are the illumination intensities as a function of wavelength using the previously-described narrow-band filters at 450, 550, 650, 750, 850, and 100 nm and the broad-band input of Figure 13. For reference purposes the normalized broad-band tungsten-light source signal is also plotted. Note that the pass-band filtered magnitudes match well with the broad-band response, and support the accuracy of the results.

By plotting the center-frequency wavelengths for the narrow-band data of against the against the median filter-wavelength for each bandpass filter, the x-axis (wavelength) calibration is established. Figure 16 plots this result. On Figure 16, the red symbols represent the x-axis (wavelength) locations of the median filtered amplitudes for each of the pass-band filters. The blue symbols represent the x-axis locations of the peak output amplitude, and the dashed line represents a linear curve fit of the median filtered amplitude data.

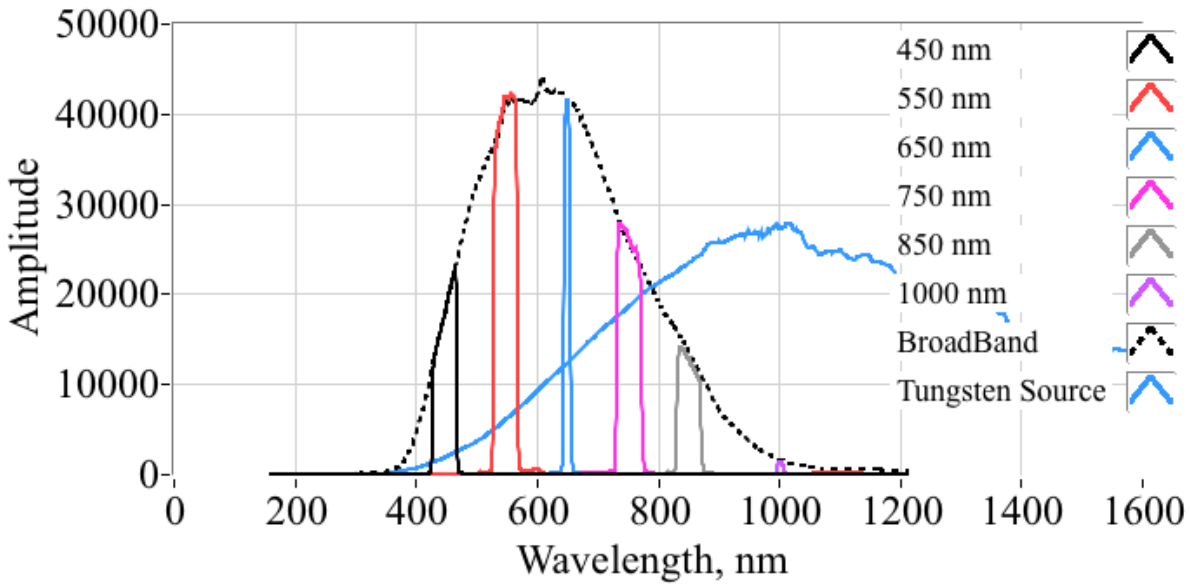

Figure 15. Band-pass filtered and wide-band responses of LR-1 with Newport clear fiber-optic cable at visible /near-IR wavelengths.

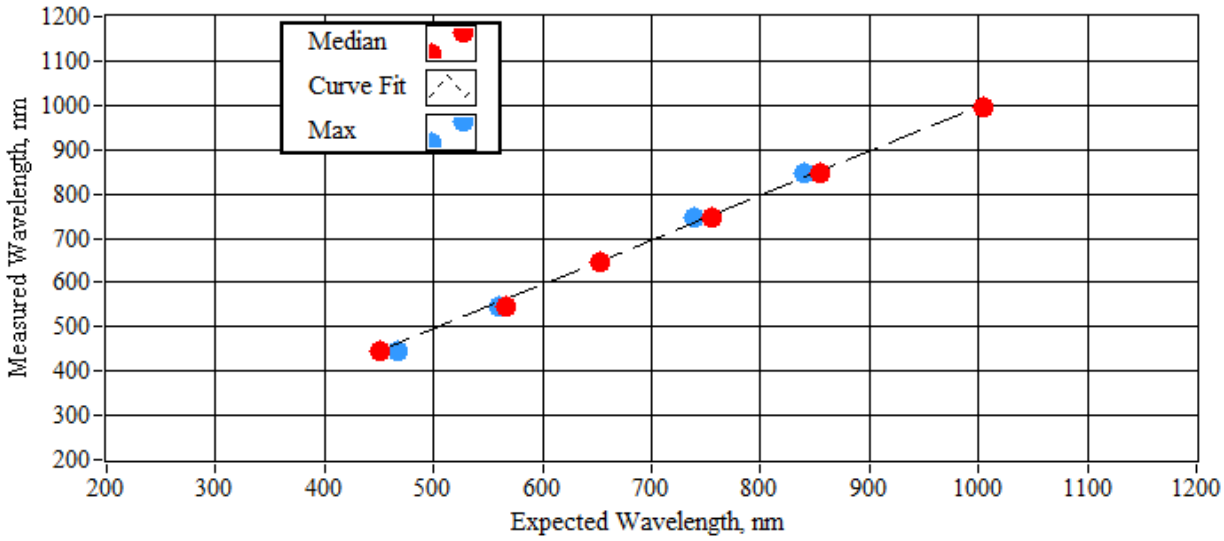

Figure 16. Wavelength calibration for LR-1 with Newport clear fiber-optic cable.

The calibrations show a nearly 1-1 results with the associated linear curve fit being,

$$\lambda_{sensed} = 1.0029 \cdot \lambda_{refernce} - 5.687_{nm} \quad . \tag{15}$$

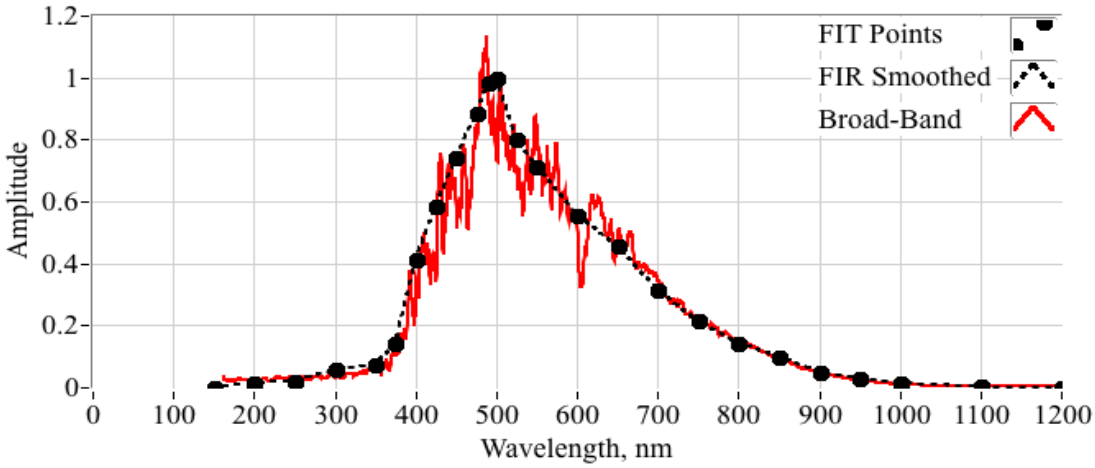

Figure 17. Normalized signal-to-noise ratio spectrum for LR-1 with Newport clear fiber-optic cable.

Figure 17 shows the estimated signal-to-noise ratio for the LR-1/Newport-clear cable arrangement, as estimated using the method of Eqs (8)–(10). Figure 17 plots the raw data as a solid red-line. The dashed black line plots data smoothed using the previously-described FIR filter. The black symbols are the smoothed-data, thinned to give a two dimensional table of breakpoints. The data are normalized to give a peak (smoothed) magnitude of 1.0. Note that the peak signal strength is near 500 nm wavelength points, with a rapid drop-off at wavelengths below 350 nm and above 900 nm. This useful range is significantly smaller than the manufacturer's specified wavelength range [28].

As derived in a similar manner to the previous example, Figure 18 shows composite calibration results for the LR-1 when coupled with the Thor Labs-blue fiber-optic cable, from Table 3. Figure 19 shows the associated x-axis wavelength calibration. Note that the Thor Labs Blue cable exhibit a slightly greater attenuation than does the Newport cable.

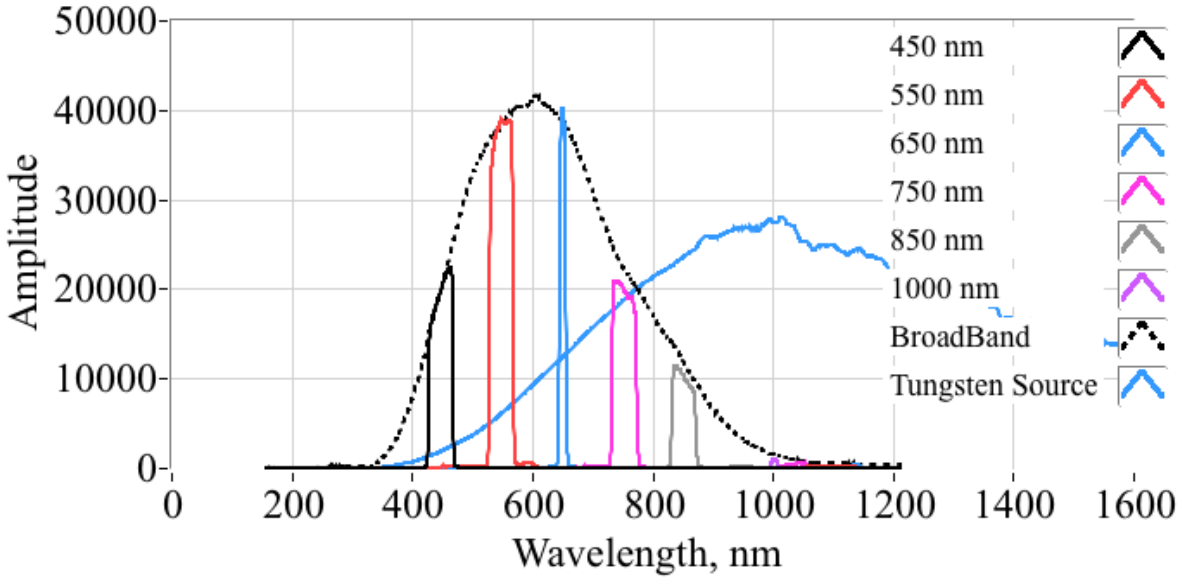

Figure 18. Band-pass filtered and wide-band responses of LR-1 with Thor-Labs blue fiber-optic cable at visible/near-IR wavelengths.

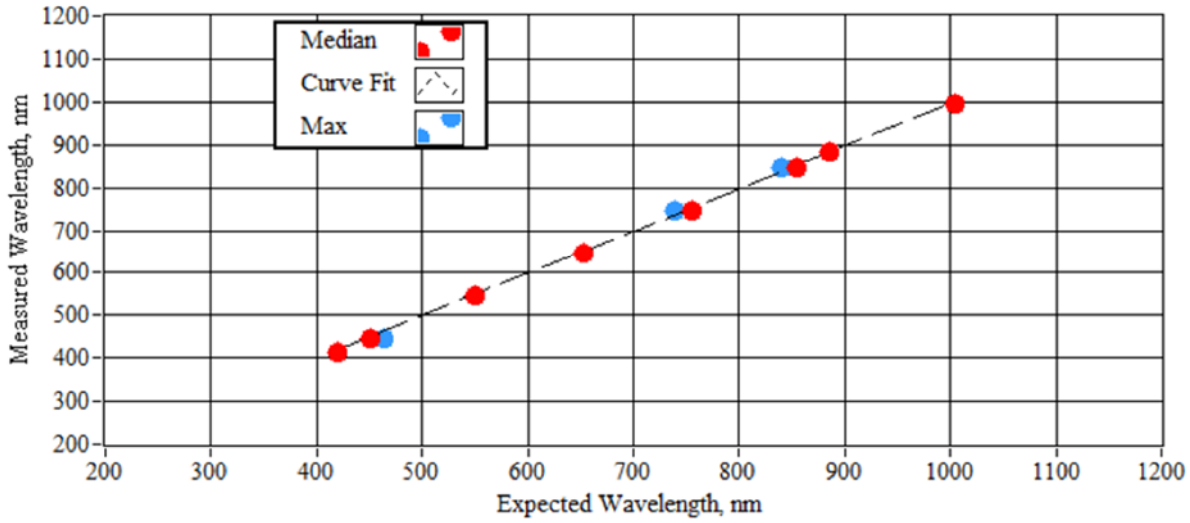

Figure 19. Wavelength calibration for LR-1 with Thor Labs blue fiber-optic cable.

The linear curve fit for this data set is,

$$\lambda_{sensed} = 0.9912 \cdot \lambda_{refernce} + 4.665_{nm}. \tag{16}$$

Figure 20 shows the estimated (normalized) signal-to-noise ratio for the LR-1 Thor Labs-blue cable arrangement. Here the plotted curves are the same as for the precious example. The dashed black line plots data smoothed using the previously-described FIR filter. The black symbols are the smoothed-data, thinned to give a two dimensional table of breakpoints. The normalized signal-to-noise ratios for the two LR-1 arrangements are essentially identical.

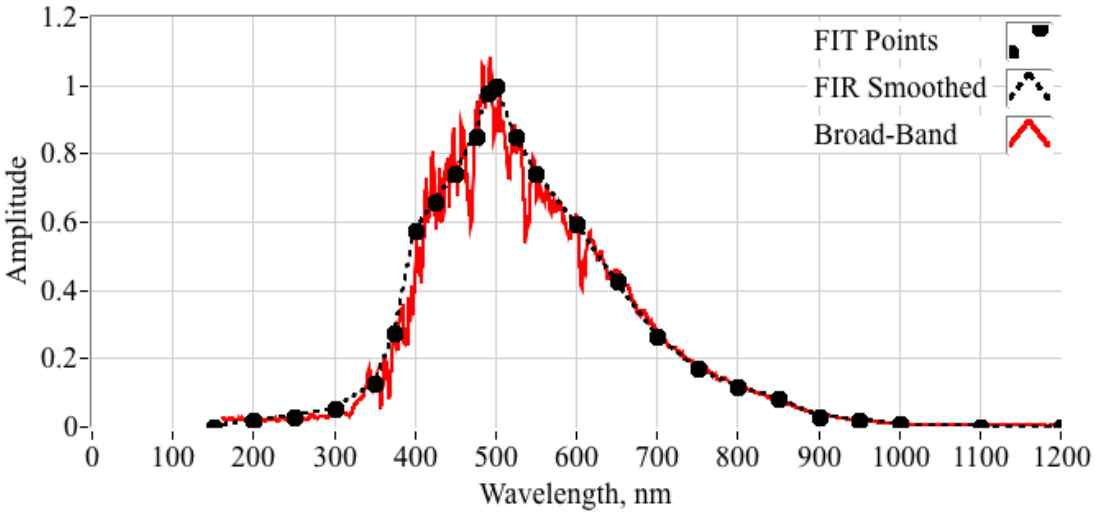

Figure 20. Normalized signal-to-noise ratio spectrum for LR-1 with Thor Labs blue fiber-optic cable.

5.1.2. QNEO IR calibrations

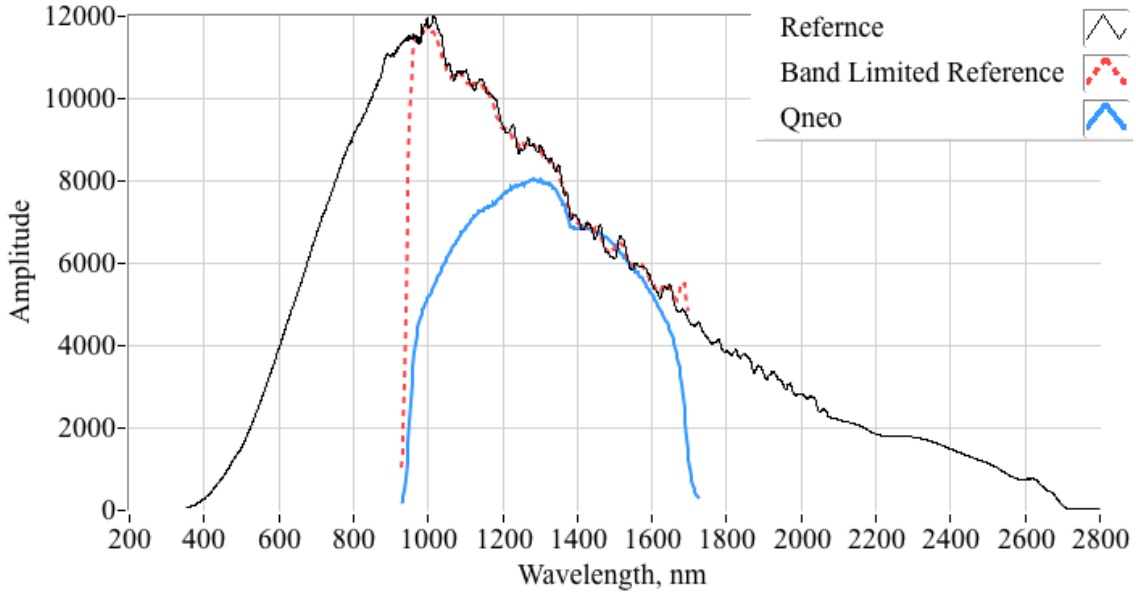

Figure 21. Wide-band response of QNEO with Thor Labs blue-orange fiber-optic cable at IR wavelengths.

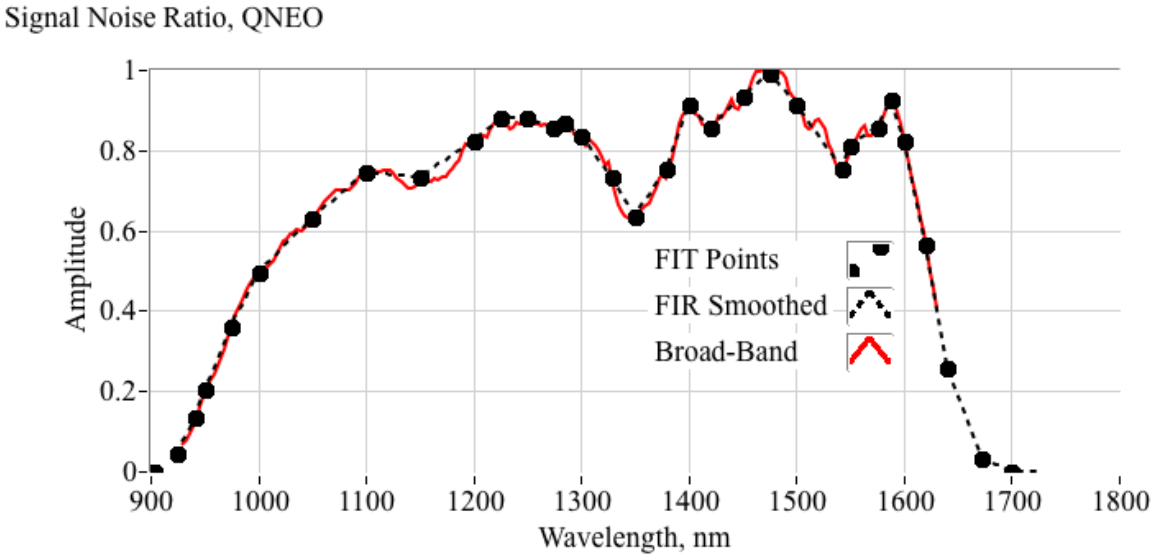

Figure 22. Normalized signal-to-noise ratio spectrum for QNEO with Thor Labs blue-orange fiber-optic cable.

As described previously, due to the lack of reasonably priced narrow-band IR-filters compatible with the SLS201L tungsten light source, the Broadcom QNEO spectrometer was calibrated using only the wide-band SLS201L input, optically filtered to remove visible light. Figure 21 shows the calibration results where the QNEO spectrometer is coupled with the Thor Labs Blue-Orange cable (from Table 3). Shown are the SLS201L tungsten light-source input (black line), the filtered source input (red-dashed line), and the NEO response (blue line). Because the no narrow-band filtered data was

available for the IR-spectrum, the x-axis (wavelength) calibration was assumed to be unity. Figure 22 shows the estimated signal-to-noise ratio over the IR-spectrum. Note that the output signal strength drops off rapidly at wavelengths above 1650 nm. Once again the observed useful range of the QNEO spectrometer is considerably more narrow than the manufacturer's specified operating range.

5.1.3. Hamamatsu C13985 radiometric calibration

A calibration of the Hamamatsu spectrometer was performed using the SLS201L tungsten light source was attempted; however, the source light was too powerful for the C13985 spectrometer, and the output signal saturated for most of the visible light spectrum. An attempt was made to attenuate the signal using the previously-described optical attenuators, but this addition resulted in a seriously compromised output spectrum. Thus, for the few C13985 data cases to be presented in this report, the manufacturer-provided sensitivity/transfer function was used, Ref [25, pp. 2–3] For any calculations performed using C13985, the assumed signal to noise ratio is 100% for all wavelengths, i.e. Wiener-filtering is not performed.

Radiometric calibration summary

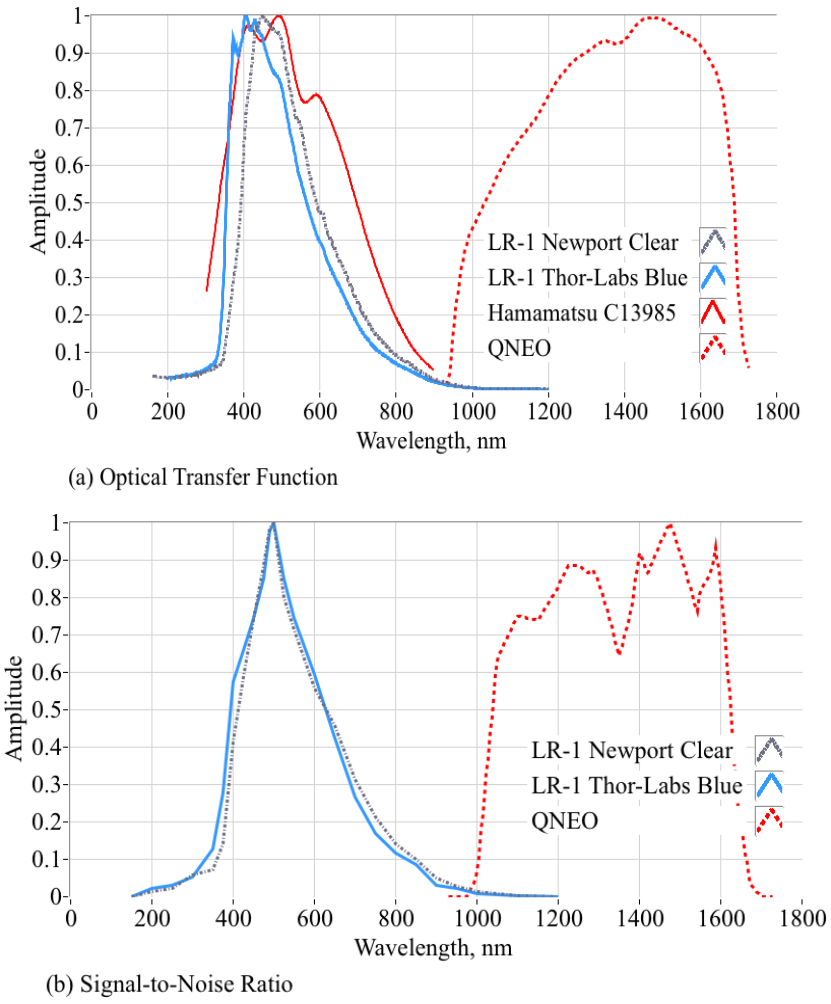

Figure 23. Radiometric calibration summary, sensitivity/transfer functions and S/N ratio models for visible, near-IR, and IR spectra.

Figure 23 summarizes the radiometric calibration results. In calculating the system transfer functions from the calibration data, both the measured spectrometer response and the tungsten light-source reference signal were smoothed using identical FIR lowpass filters. Figure 23(a) compares the transfer functions for the LR-1/Newport-clear, LR-1Thor Labs-Blue, Hamamatsu C13985 and QNEO arrangements, and Figure 23(b) displays the corresponding signal-to-noise ratio models. Per the previous discussion, a S/N estimate for the Hamamatsu C13985 was not available, and is not plotted. Two impotent observations can be made with regard to the resented data. First, although some differences exist, the visible-light arrangements all have generally the same transfer function properties, thus the cable selections did not appreciably influence the archived spectra. Second, and more importantly, there exists a distinct "wavelength-gap" between 800 and 950 nm for the combined visible-light (LR-1, C13985) and near-IR (QNEO) sensing arrangement. Unfortunately, as shown by Figure 3, this gap also coincides with the peak-magnitude (Wien's Law) wavelengths for the combustor flame-temperature. Thus, thus transfer function characteristics are not ideal for the proposed dual-band system. The manufacturer's overly-optimistic operating range specifications that lead to system defect. Unfortunately, this behavior was not discovered until the testing campaign was well under-way, and schedule and budget constraints did not all the procurement of alternative hardware. As will be shown later in the results section, this "wavelength-gap" did not prove to be a critical system flaw, and the splicing technique as described in Section 4.4.4 was able to work-around this defect.

5.2. Hot fire test results

This section presents the results of the hot fire testing campaign. To date more than 50 successful burns have been performed with the fiber-optic sensors installed. Both-single band (Visible Light) and Dual-Band (Visible Light, Near-IR) data were collected. Most of the early tests used single-band visible light spectrometers, both the C13985 and LR-1. The final grouping of 20 tests were performed using the dual-band (LR-1, QNEO) sensor arrangement. A majority of the presented test data here were acquired using the 75 mm thrust chamber of Figure 6. However, in support of another project, a few tests with fiber-optic chamber measurements were performed using a 98 mm motor of similar design, and for completeness, these results are also reported here.

5.2.1. Fiber optic cable survival

As described in the introductory sections, the optical systems were designed with the expectation of the fiber-optic cable burning away over the course of the burn, while still transmitting light. Generally, this expectation was satisfied; however, there are some useful post-burn observations about the state of the fiberoptic cables. Figure 24 shows the post-burn fiber-optic cables tips for both the combustion chamber and the nozzle exit plane.

Figure 24(a) presents a view looking downstream into the disassembled, extruded-portion of the fuel grain, showing the tip of the fiber (Newport Clear) slightly protruding and covered with soot. Generally, this slight protuberance did not create an issue with erosive burning; however, the deposition of soot did noticeably lower the sensed optical intensity near the end of longer duration burns. This effect was especially noticeable for low O/F ratio burns. Fortunately, it appears that the lowered intensity did not noticeably shift the spectrum wavelengths, likely allowing accurate flame temperature measurements throughout the burn duration. Test results demonstrated that the chamber fiber-optic

survived intact and transmitting for burn durations as long as 25 seconds.

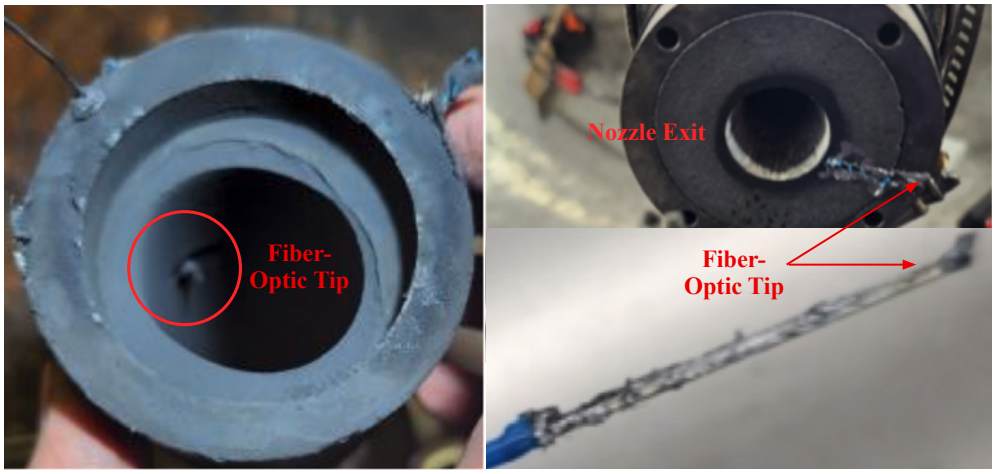

(a) Thrust Chamber Fiber Optic (b) Nozzle Exit Fiber Optic

Figure 24. Post-burn images of combustion chamber and nozzle exit fiber optic cable tips.

Figure 24(b) presents an external view of the nozzle exit plane with the fiber-optic retaining clamp removed from the motor. Pictured is the fiber-optic (Thor Labs, blue) showing the fiber-tip. Notice that, even though the cable was initially installed so as to protrude into the exhaust plume flow, post-burn the cable tip has burned back nearly to the nozzle wall and the external sheath (blue) is charred or burned away. Even so, the cable core remained intact and transmitted light throughput the burn, even after 25 seconds of total-burn duration. Unlike the combustion chamber fiber, the exit plane fiber does not become covered in soot, and transmits a constant optical intensity throughout the burn.

5.2.2. Presentation of hot-fire burn examples

Results from the testing campaign are best shown through by 3 representative examples, two with constant throttle settings at 100% and 50%, and one example with a deep throttle where the motor is throttled from 100% to 30% and back to 100% over 10-second time period. Deep-throttling allows a range of O/F ratios to be observed during a single burn. For each example, dual band (LR-1 and QNEO) spectrometer data are available, and are correlated to the presented performance data. In order to better-understand the effectiveness of the dual-band system, for the first example the dual-band spectra and associated flame temperature solutions are also compared to spectra and flame-temperature solutions as calculate using only the visible-light (LR-1) data. For both the visible-light and IR sensors, each spectrum output was time-tagged and logged for later correlation to the motor performance data.

Table 4 summarizes the presented data parameters. Under the Planck's law Column of Table 4, the parameter K is the optimal QNEO Scale factor (from Eq (14)), A is the Plank's Curve amplitude, and T is the fit-temperature. Under the Wien's law Column of Table 4, the parameter λ_{max} is the wavelength at which the maximum spliced-curve data amplitude occurs, and T is the corresponding black-body temperature. For Example, 3 the labeled rows, 3(a), 3(b), and 3(c), correspond to data for the 100%, 30%, and 100% throttle settings.

Table 4. Summary of presented examples.

Example No.	Motor (Throttle)	Mean O/F	Planck's Law Fit Parameters			Wien's Law Fit Parameters		CEA Flame Temperature
			K	*A*	*T*, K (°C)	λ_{max} nm	*T*, K (°C)	*T*, K (°C) $\eta^* = 100\%$
1	75-mm, Long (100%)	1.28	17.51	259.2	3059.8 (2786.7)	1150	3046.0 2772.9	3023.15. (2750)
2	Short (50%)	3.40	1.363	213.4	3155.8 (2882.7)	913	3173.9 (2900.8)	3373.15 (3100)
3(a)	75-mm, Long (100%) (1)	1.70	1.376	223.2	3259.7 (2986.5)	884	3278.0 (3004.9)	3323.15 (3050)
3(b)	75-mm, Long (100%) (1)	0.89	90.04	4590.8	2167,65 (1894.5)	1314	2178.8 (1905.6)	2223.2 (1950)
3(c)	75-mm, Long (100%) (2)	1.18	29.66	1020.8	2665.7 (2392.6)	1081	2680.6 (2407.5)	2723.15 (2450)

Example 1: 75-mm motor, long-grain, constant full-throttle (100%) burn

In order to give a clear picture of the analysis process, this first example will be walked-through in detail. The motor performance data is presented first, followed by the optical data analysis. This test started with a longer full-length fuel-grain of Figure 7(a) that has not been previously burned. Since O/F ratio has a strong influence on the flame temperature, the primary task of the motor performance data is to anchor O/F ratio over the burn duration. Figure 25 shows the performance analysis. For this example, the digital throttle system was commanded to throttle the motor at 100% for the full 8-second burn duration. Plotted are (a) commanded throttle, (b) thrust as sensed by the load cell and also as calculated from the chamber pressure measurement, (c) injector and chamber pressure, (d) oxidizer, total, and fuel massflow rate, (e) O/F ratio (both mean and instantaneous), and (g) the combustor (flame) and nozzle exit temperature estimates (from CEA). The plotted flame temperatures are calculated from the previously-described CEA tables, using the measured chamber pressure and both the instantaneous (shifting) and mean O/F ratios over the burn duration. Using the previously-described De Laval Flow, Ref [42], assuming adiabatic nozzle flow, the nozzle exit temperature is also estimated from the CEA tables.

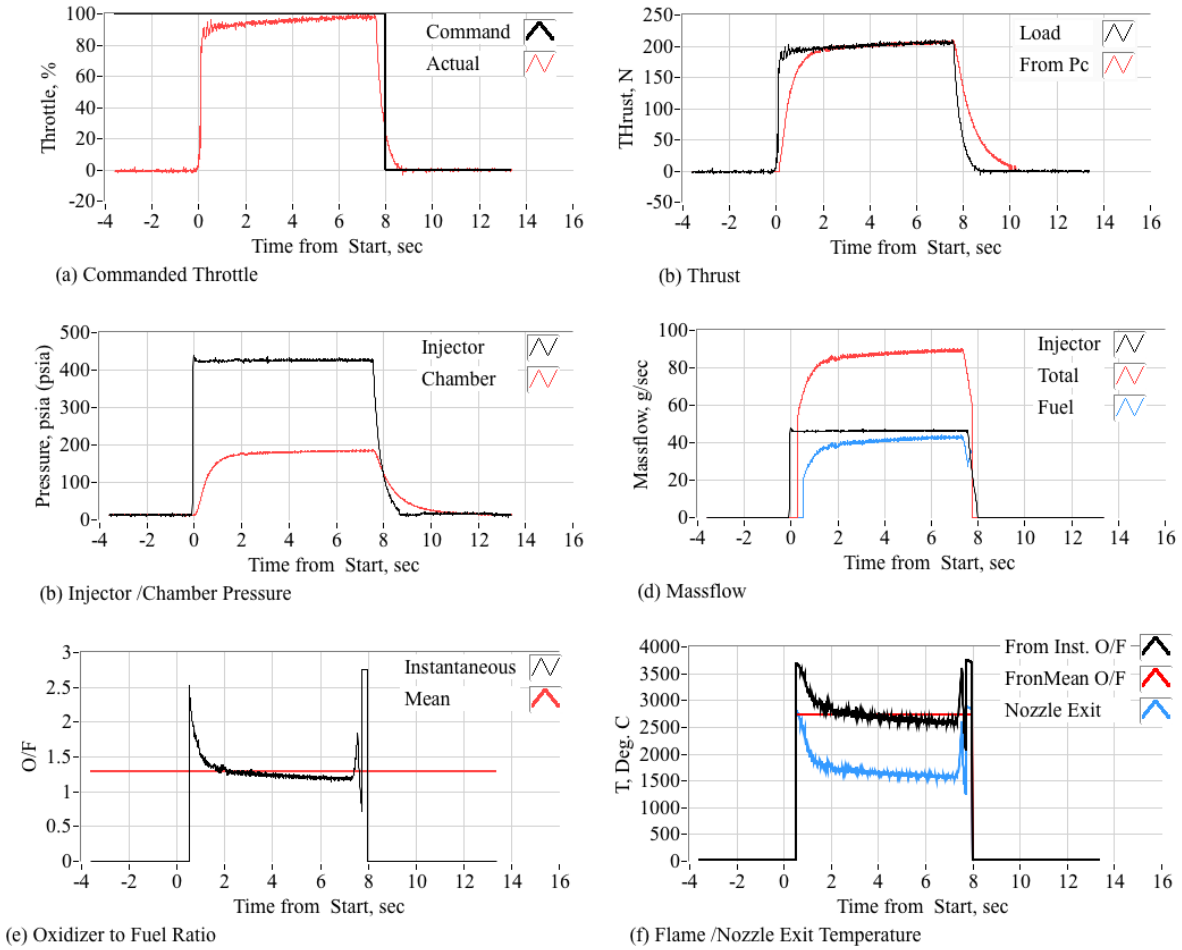

Figure 25. Example 1, 100% throttle, 75-mm, long grain, hybrid motor performance analysis.

Note, that the motor thrust increases by approximately 7% over time even though the commanded throttle level remains fixed at 100%. This thrust-growth event is due to a lean-to-rich O/F shift, which results an increase in the pyrolyzed fuel massflow, even though the oxidizer mass flow remains constant through the burn duration. Ziliac and Karabeyoglu [45] describe this O/F shift process in detail. The O/F shift comes from a decreasing oxidizer massflux over time, traded-off against an increasing fuel burn area. Appendix 2 presents additional information with regard to the fuel pyrolysis and the lean-to-rich O/F shift experienced by the 75-mm thrust chamber. This O/F-shift behavior is well understood for the 75-mm test article and has been previously reported by Whitmore and Merkley [46].

The mean flame temperature and O/F ratio, calculated across the entire burn time history, are now correlated to the optically sensed flame temperature. The presented spectra are average from three optical frames, chosen midway through the full throttle. At this point in the burn, based on both the mean O/F ratio, assuming 100% combustion efficiency, the CEA predicted Flame Temperature is approximately 2750 °C (3023.15 K). Figure 26 first plots (a) the raw LR-1 visible/Near-IR, and (b) LR-1 spectrum adjusted by the transfer function. Figure 26(b) plots two curves, the black curve is the LR-1 spectrum adjusted by dividing the transfer function through at each wavelength *(analytical deconvolution)*; the red curve is the LR-1 spectrum adjusted using Wiener filtering, accounting for signal-to-noise ratio *(optimal deconvolution)*.

Figure 26(c),(d) feature the same plot descriptions, except now the QNEO Near-IR/IR spectra are

plotted. In this figure the black line represents the deconvolved signal using the Wiener filter, and the dashed red-lines are the analytically-adjusted spectrum. For analytical deconvolution the Wiener Filter does not weight the data for the effects of signal-to-noise ratio. From these plots, the advantages of using the Wiener filter to perform the optimal deconvolution are clear. Without the filter selection, the "out-of-bounds" data simply wanders-off from the nominal condition.

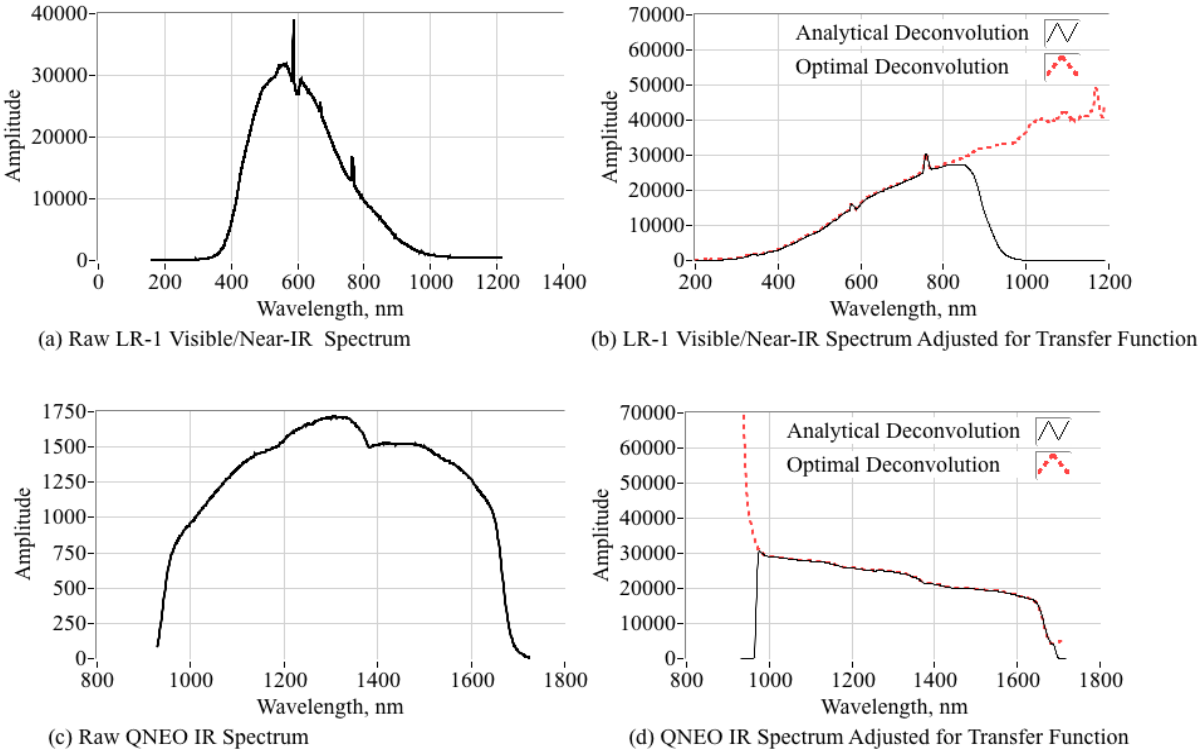

Figure 26. Example 1, LR-1 visible/near-IR and QNEO IR spectra, raw and adjusted for transfer function.

In order to complete the entire Visible/IR spectrum, the optimally-deconvolved signals from Figure 26(b),(d) are Spliced together by the previously-described process. First, the radiometrically-adjusted QNEO spectrum is multiplied by a range of scale factors. The scaled IR-data (QNEO) are then concatenated with the radiometrically-adjusted visible (LR-1) spectra, and curve fit to Planck's law. The scale factor allowing the minimum variance fit is the optimal-solution. Figure 27 shows this process. Figure 27(a) compares the LR-1 visible spectrum with the QNEO IR-spectra scaled by various values of *K*. Figure 27(b) plots the Planck's Law curve fit variance (residue) against the scale factor values.

For this example, the minimum-variance is reached at a value K = 17.51. Figure 27(c) shows the spliced spectrum using the optimal scale factor, interpolated to a constant wavelengths. Finally, Figure 27(d) shows the optimal fit, with the narrow-band peak at 747 nm (likely due to nitrogen), "notched" out using a band-rejection filter as described by Ref [44]. For the optimally-spliced data, the temperature is calculated in two ways, 1) the Temperature T from the Planck's law curve fit, and 2) the temperature calculated from Wien's law, applied at the peak-amplitude wavelength of the spliced spectrum. Generally, these two-estimates are found to agree within approximately 10–12 ℃. As shown by Table 4, from the curve fit of Figure 27(d) the black body temperature from the Planck's law curve fit is calculated to be 3059.8 K (2786.7 ℃), and from Wien's law is calculated to be

approximately 3046.0 K (2772.9 ℃). The curve-fit values agree within 40 °C (1.2%) of the mean CEA-derived temperatures (3023.2 K, 2750 ℃), as plotted by Figure 25(f).

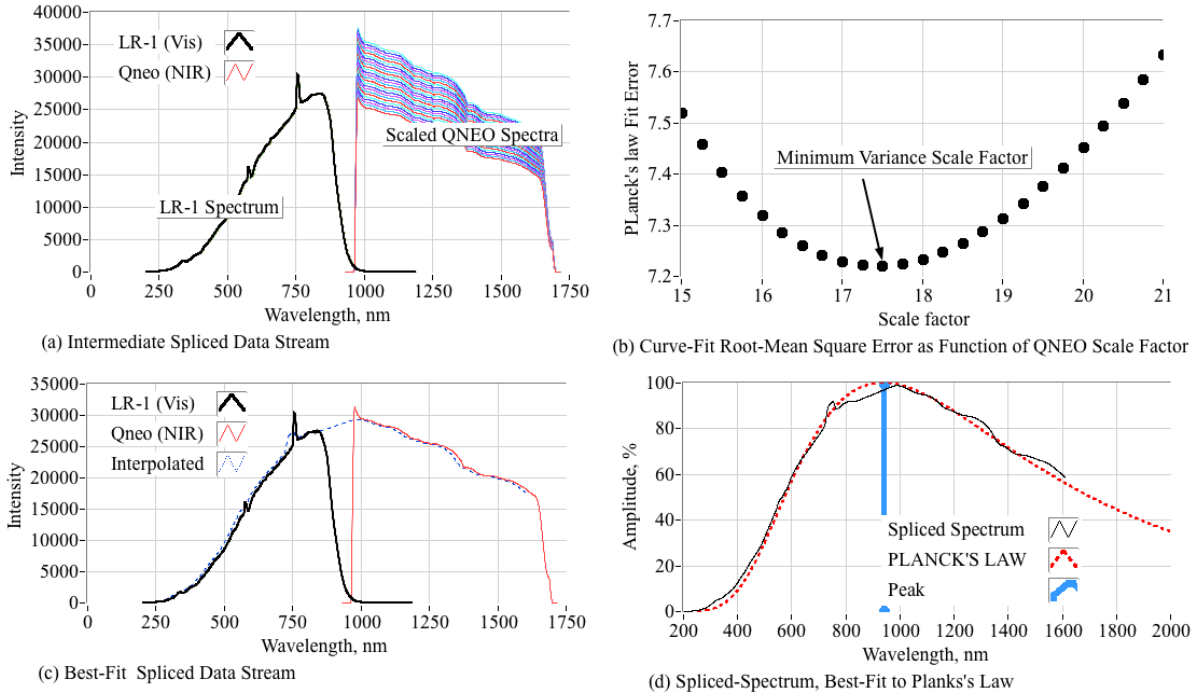

Figure 27. Example 1, optimally spliced visible (LR-1) and IR (QNEO) spectra, curve fit to Planck's Law.

As an illustration of the utility of the dual-band curve fit, Figure 31 shows the Planck's Law curve fit using only the LR-1 visible spectrum data. This "one-sided" single-band curve-fit shows that the LR-1 data is quite reliable up to about 850 nm, but well below the black-body peak wavelength. Due to the curve-fit extrapolation, the 1-sided spectrum predicts a Planck's Law flame temperature is significantly higher than calculated using the dual-band spectrum, approximately of 3096.2 K (2823.0 °C). Because the data does not capture the black-body peak, Wien's law cannot be used to estimate the flame temperature. These values more than 50 °C higher than the values as calculated using the dual-band Spliced spectrum.

Example 2: 75-mm motor, long-grain, constant half-throttle (50%) burn

This example presents the constant 50%-throttle burn, with the short-grain configuration of Figure 7(b) replacing the longer motor in order to achieve a higher O/F ratio. Figure 29 shows the resulting motor performance data. Note that for this burn the achieved thrust is very nearly 50% of that as achieved by the burn of Figure 25. Also note, due to the shortened fuel grain, the O/F ratio is now considerably higher, approximately 3.40, and the associated flame temperature is now approximately 3372.2 K (3100 ℃).

Figure 30 shows the optimally-spliced spectrum data for this burn. Once again the curve fit is excellent, and the corresponding's Planck's Law temperatures are 3155.8 K (2882.7 ℃), and from Wien's law is approximately 3173.9 (2900.8 ℃). When compared to the CEA-derived values for the O/F ratio, these values are 200 ℃ or approximately 6.5% lower.

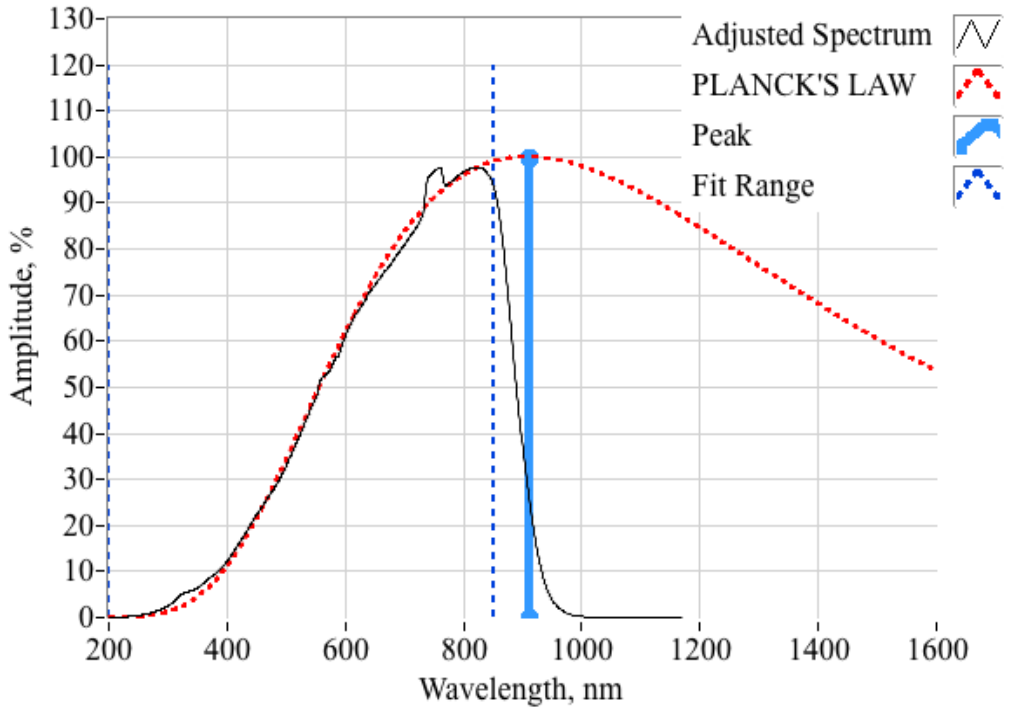

Figure 28. Example 1, Planck's Law curve fit using "one-sided" LR-1 visible light spectrum.

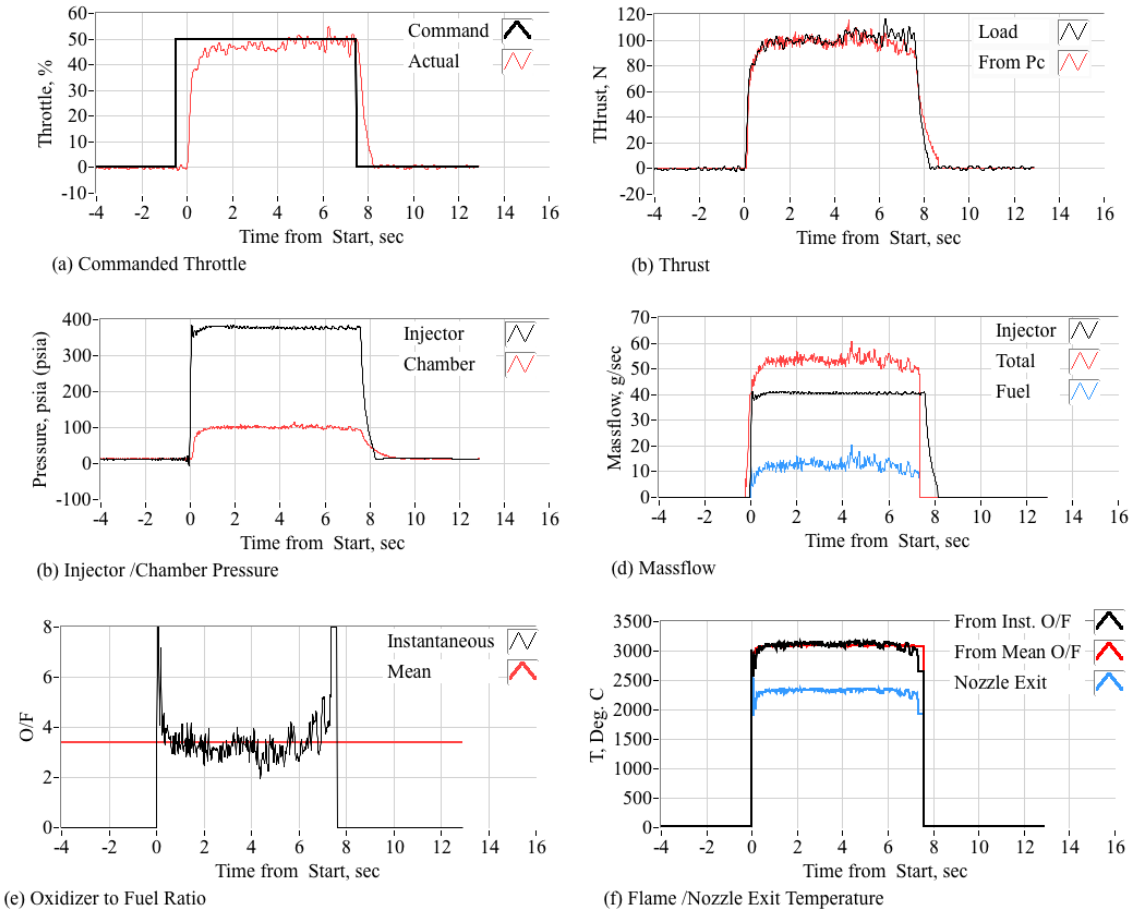

Figure 29. Example 2, 50% throttle, short grain, hybrid motor performance analysis.

Similar to the data of Figure 28, Figure 31 shows the Planck's Law curve fit for the data of Figure 30 using only the one-sided LR-1 visible-light spectrum. As before, the extrapolation leads to an over-predicted temperature estimate, approximately 3237.9 K (2964.8 °C). This value is more than 80 °C higher than the dual-band spectrum calculation.

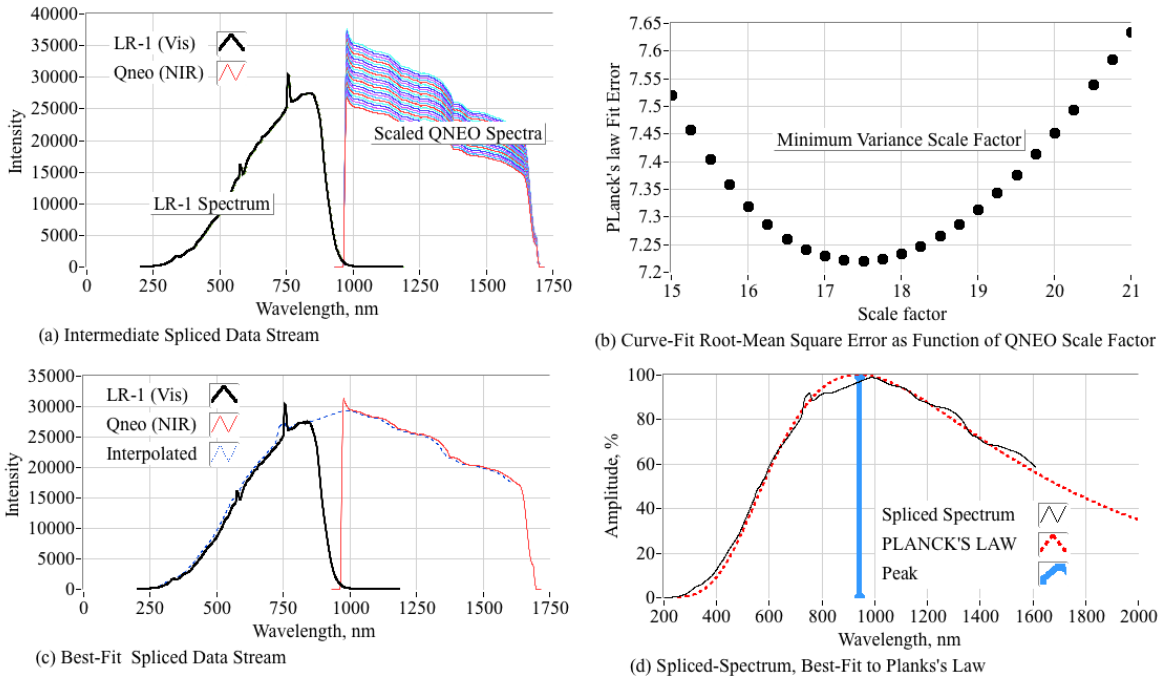

Figure 30. Example 2, optimally spliced visible (LR-1) and IR (QNEO) spectra, curve fit to Planck's Law.

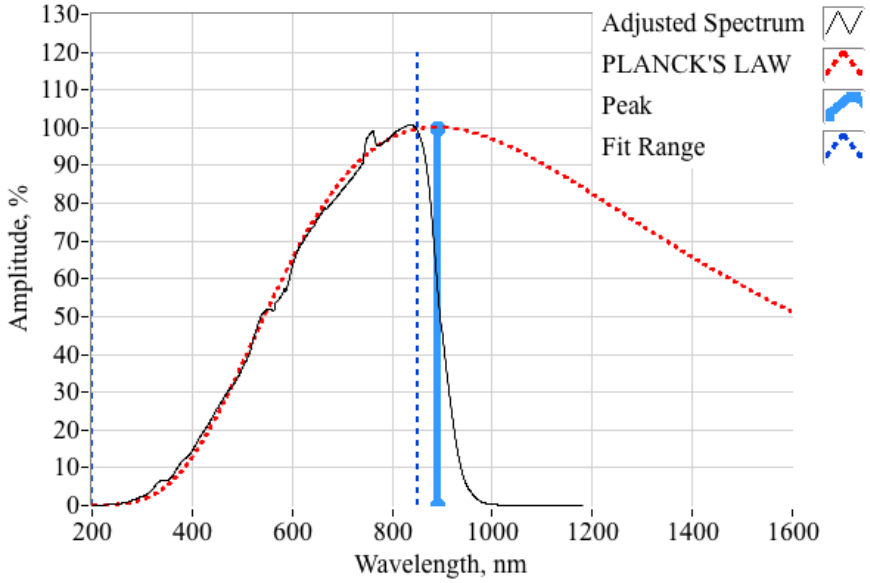

Figure 31. Example 2, Planck's Law curve fit using "one-sided" LR-1 visible light spectrum.

Example 3: 75-mm motor, long-grain, deep-throttle profile

For this example, the long-grain motor was deeply throttled from 100% to 30% and back to 100%

over 10-second time period. As described earlier, deep-throttling allows a range of O/F ratios to be observed during a single burn. For this test, as noted by the differences in the two maximum thrust "humps" at the beginning and end of the burn, the motor undergoes a very strong O/F shift. The O/F ratio varies from approximately 1.7 at the beginning of the burn to less than 1.0 at the minimum throttle, and back to approximately 1.15 by the burn's end. The associated CEA flame temperatures are calculated to vary from 3050 ℃ to less than 2000 ℃ and back up to approximately 2450 ℃. The considerably lower final flame temperature for this burn is due to the large O/F shift during the burn. The flame temperature based on the mean O/F ratio, approximately 1.30, is 2740 ℃. The wide range of O/F ratios gives the opportunity to examine multiple spectra throughout the burn, with the intent to verify that the dual-band optical system can detect the changing flame temperatures. Spectra data collected at three stages during the burn, 1) initial 100% throttle, 2) 30% throttle, and 3) final 100% throttle are presented by Figures 33–35. Because of the slow response rate of the QNED spectrometer, only 5 IR data frames were collected over the entire burn, and frame-averaging was not available for this throttled data. QNEO frame-1 was used for the initial 100% throttle setting, frame-3 was used for the 30% throttle setting, and frame-5 was used for the final 100% throttle setting.

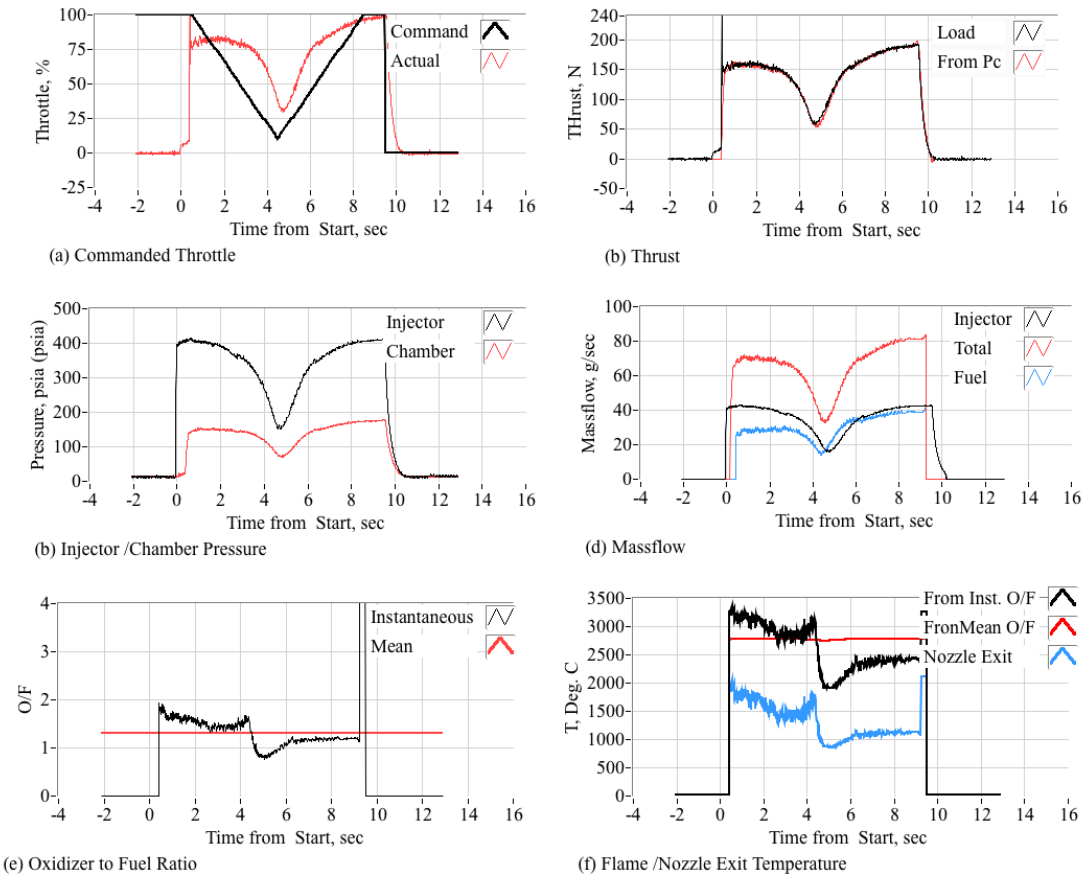

Figure 32. Example 3, deep-throttle throttle, 75-mm, long grain, hybrid motor performance analysis.

Example 3, initial 100% throttle spectrum analysis.

Figure 33 shows the optimally-spliced spectrum data for the first 100% throttle setting, collected approximately 1-second after full-burn initiation. Once again the curve fit is excellent, and the corresponding's Planck's Law temperatures are approximately 3259.7 K (2986.5 ℃), and 3278.0 K

(3004.8 ℃) from Wien's law. When compared to the CEA-derived values for the O/F ratio, these values are less 60 ℃ or approximately 2% lower.

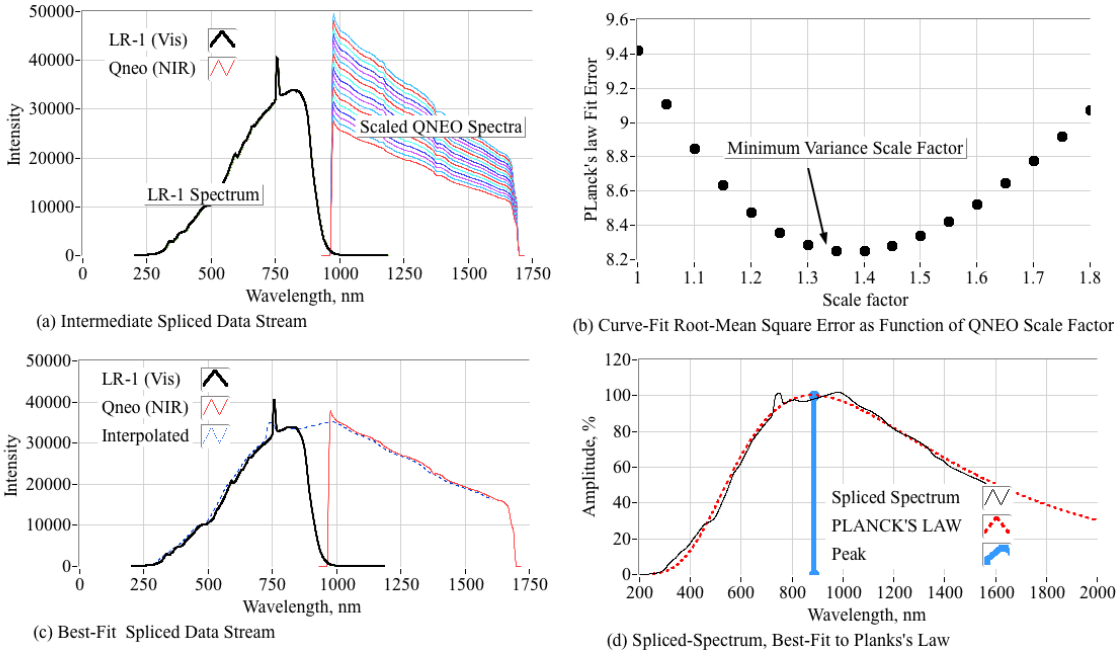

Figure 33. Example 3, optimally spliced visible (LR-1) and IR (QNEO) spectra, curve fit to Planck's Law at Initial 100% throttle level.

Example 3, middle 30% throttle spectrum analysis.

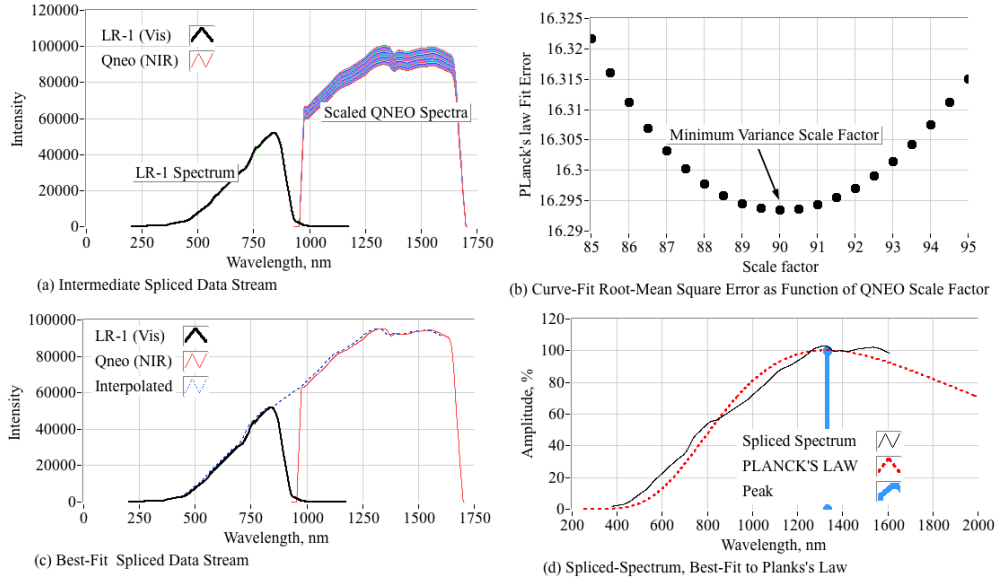

Figure 34. Example 3, optimally spliced visible (LR-1) and IR (QNEO) spectra, curve fit to Planck's Law at middle 30% throttle level.

Figure 34 shows the optimally-spliced spectrum data for the middle 30% throttle setting, collected

approximately 4.5-seconds after full-burn initiation. The corresponding's Planck's Law temperatures are approximately 2167.6 K (1894.5 ℃), and 2178.8 K (1905.6 ℃) from Wien's law. When compared to the CEA-derived values for the O/F ratio, these values are 50 ℃ or approximately 1.7% lower. For this case the curve fit is not as well-defined with respect to Planck's Law as for the previous examples. This effect is possibly due to the plume opaqueness at this fuel-rich O/F ratio, approximately 0.88.

Example 3, final 100% throttle spectrum analysis.

Figure 35 shows the optimally-spliced spectrum data for final 100% throttle setting, collected approximately 8-seconds after full-burn initiation. Once again the curve fit is excellent, and the corresponding's Planck's Law temperatures are 2665.7 K (2392.6 ℃), and approximately 2680.6 K (2407.5 ℃) from Wien's law. When compared to the CEA-derived values for the O/F ratio, these values are less 50 ℃ or approximately 2% lower.

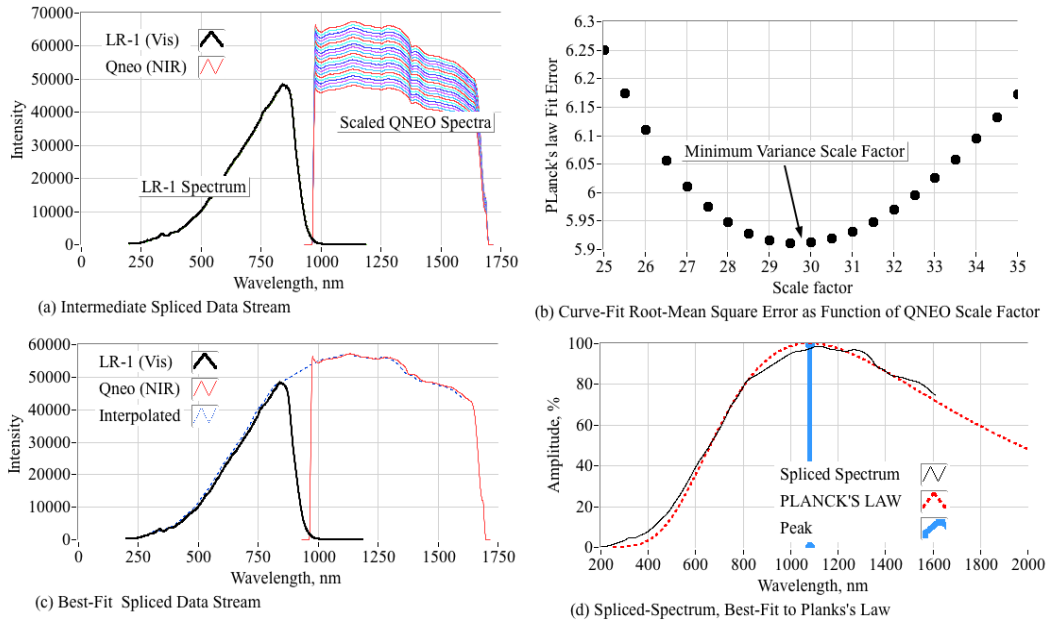

Figure 35. Example 3, optimally spliced visible (LR-1) and IR (QNEO) spectra, curve fit to Planck's Law at final 100% throttle level.

Summary of example results

Figure 36 summarizes the presented 3-example results by plotting the flame temperatures calculating using Wien's law, the Plank's Law curve-fit, and the CEA data base against the mean O/F level. Note that for the lower O/F levels, there is good agreement between the optically-sensed flame temperatures and the CEA data base calculations. However, at higher O/F ratios, the optically-sensed values are clearly lower. An explanation for this discrepancy, driven by the higher O/F ratios and associated combustor dwell-time, will be presented later the next subsection section.

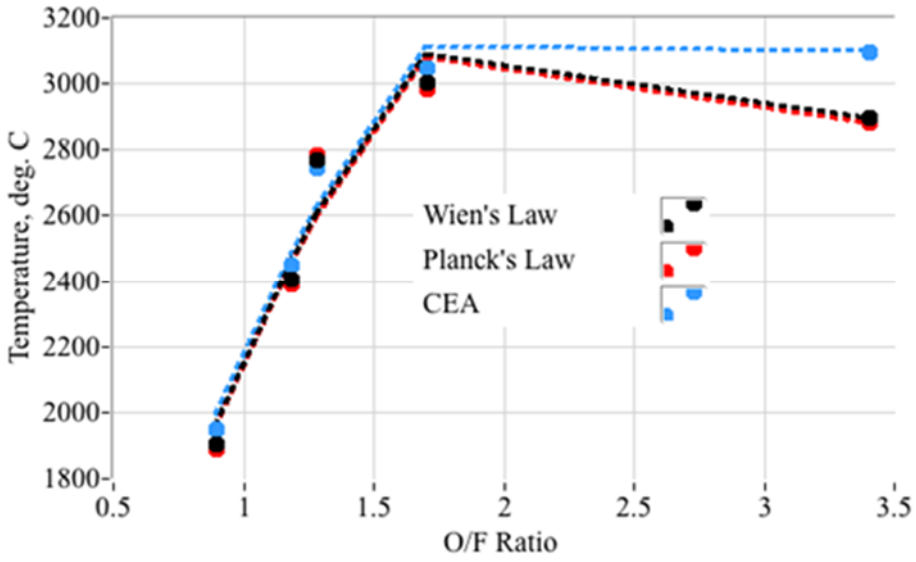

Figure 36. Section 5.2.2, summary of example results.

5.2.3. Combustion chamber flame temperature test summary

Figure 37 presents a summary of the all optically-sensed combustion chamber temperature data collected during this testing campaign. For each test condition, this figure compares the optically-sensed temperature against the 100% efficiency CEA curves for pressure levels varying from 75 psia (517 kpa) to 250 psia (1724 kpa). Data for the single-ended LR-1 and C13985 arrangements as well as the dual-band (LR-1 and QNEO) arrangement are plotted as a function of the averaged time-averaged O/F ratio. There are also three deep throttle burns, similar to the burn of Example 3, plotted in this data set. For each of the deep throttle burns, there are three points plotted, one at the initial 100% throttle, one at minimum throttle, and one at the final 100% throttle. The mean standard-deviation of the optical-data from the curve fit, plotted as the dashed black lines in Figure 37, is approximately 85 °C.

The observed trends agree well with the data as plotted by Figure 36. At the lower O/F ratios, where the burn is the most fuel-rich, the optically-sensed temperatures are equal to or slightly greater than CEA-predicted temperatures. The optically-sensed temperatures that are greater than CEA-predicted temperatures, are equivalent to a combustion efficiency greater than 100%. This discrepancy likely results from two factors. First, most of the low O/F data were sensed using only the single-band LR-1 and C13985 spectrometer arrangements. Recall that Figures 28 and 31 have previously demonstrated that, due to the extrapolation required for the peak amplitude wavelength, the single-ended data biases the temperature reading relative to the dual-band calculation. A second source for this discrepancy is that the extruded ABS fuel segment has a slightly higher enthalpy-level than the 3-D printed samples investigated during the previously-described FTIR analysis of Ref [2]. At the lowest O/F ratios, where the burn is most fuel-rich, the effects of the fuel enthalpy upon the flame temperature become amplified.

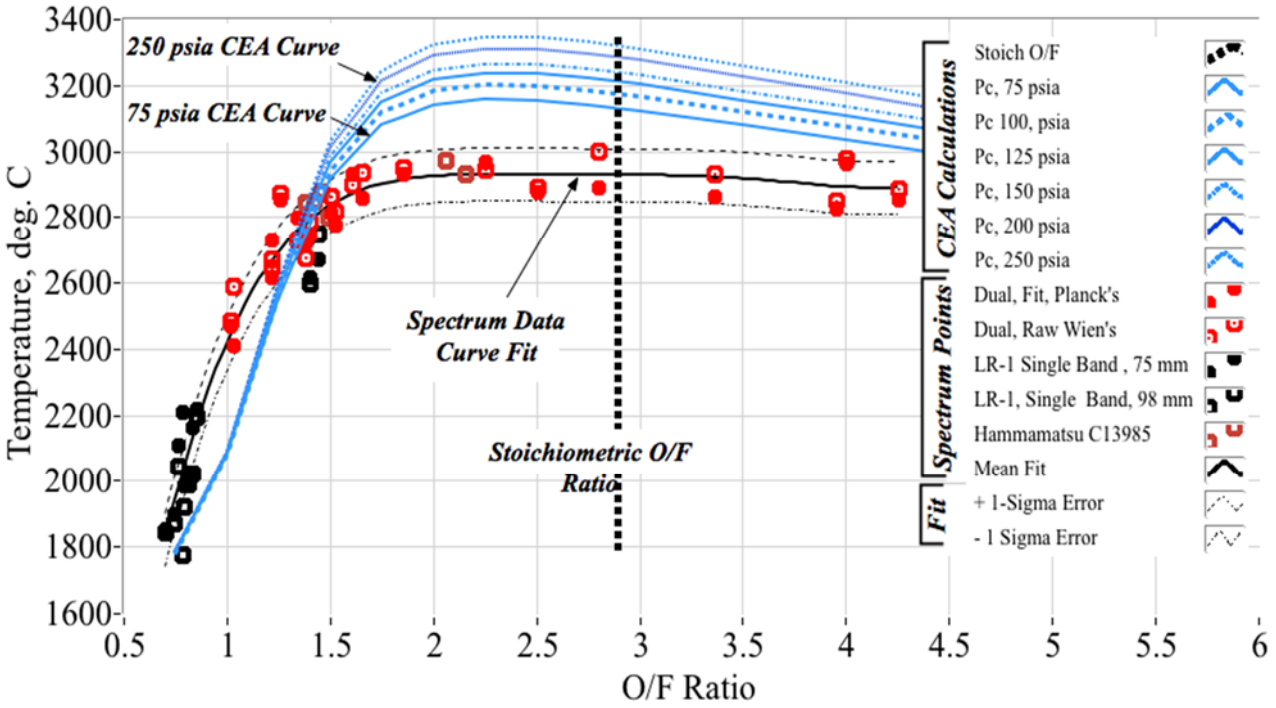

Figure 37. Optically-sensed flame temperatures as compared to theoretical (CEA) values.

At O/F ratios above 1.5 a distinct trend emerges; where, the optically-sensed flame temperatures drop away from the CEA-derived curves. Since the fuel-rich combustor plume is most-opaque, the largest temperature-sensors errors were expected at the lower O/F ratios. Thus, this observed trend was initially quite unexpected. However, when one considers the combustor dwell-time—the period of time the combustor the flow spends in the combustion chamber—as a function of O/F ratio, this trend can be explained.

Effect of O/F ratio and combustor dwell-time on combustion efficiency

As derived in Appendix 2, for a cylindrical fuel port the longitudinal mean of the fuel-port flow velocity V_{port} is correlated to O/F ratio by Eq (17),

$$V_{port} = \frac{\left(O/F \cdot \left(a \cdot \rho_f \cdot L \right) \cdot \left(\frac{1}{D_{port}} \right)^{2n-1} \cdot \left(\frac{\pi^{n-1}}{4^n} \right) \right)^{\frac{1}{1-n}}}{\rho_{ox} \cdot \frac{\pi}{4} D_{port}^2} . \tag{17}$$

Thus, the flow combustor dwell time can be written explicitly in terms of O/F ratio as,

$$\tau_{dwell} = \frac{L}{V_{port}} = \frac{L \cdot \rho_{ox} \cdot \frac{\pi}{4} D_{port}^2}{\left(O/F \cdot \left(a \cdot \rho_f \cdot L \right) \cdot \left(\frac{1}{D_{port}} \right)^{2n-1} \cdot \left(\frac{\pi^{n-1}}{4^n} \right) \right)^{\frac{1}{1-n}}} . \tag{18}$$

Approximating the combustion efficiency by the ratio of the optically-sensed (actual) flame temperature and the CEA-derived (theoretical) flame temperature,

$$\eta^*_{combustor} = \sqrt{\frac{T_{optical}}{T_{\substack{flame \\ theory}}}}, \tag{19}$$

the mean flow velocity and combustion efficiency can be plotted as a function of O/F Ratio and the combustor dwell time. Replotting the data of Figure 37, Figure 38 shows this result. As shown by Figure 38(c) the optically-sensed temperature drop-offs sharply from nearly 100% at the lowest O/F values to just-above 90% at the highest O/F values. From Figure 38(d), this drop-off is inversely correlated with the combustor dwell time.

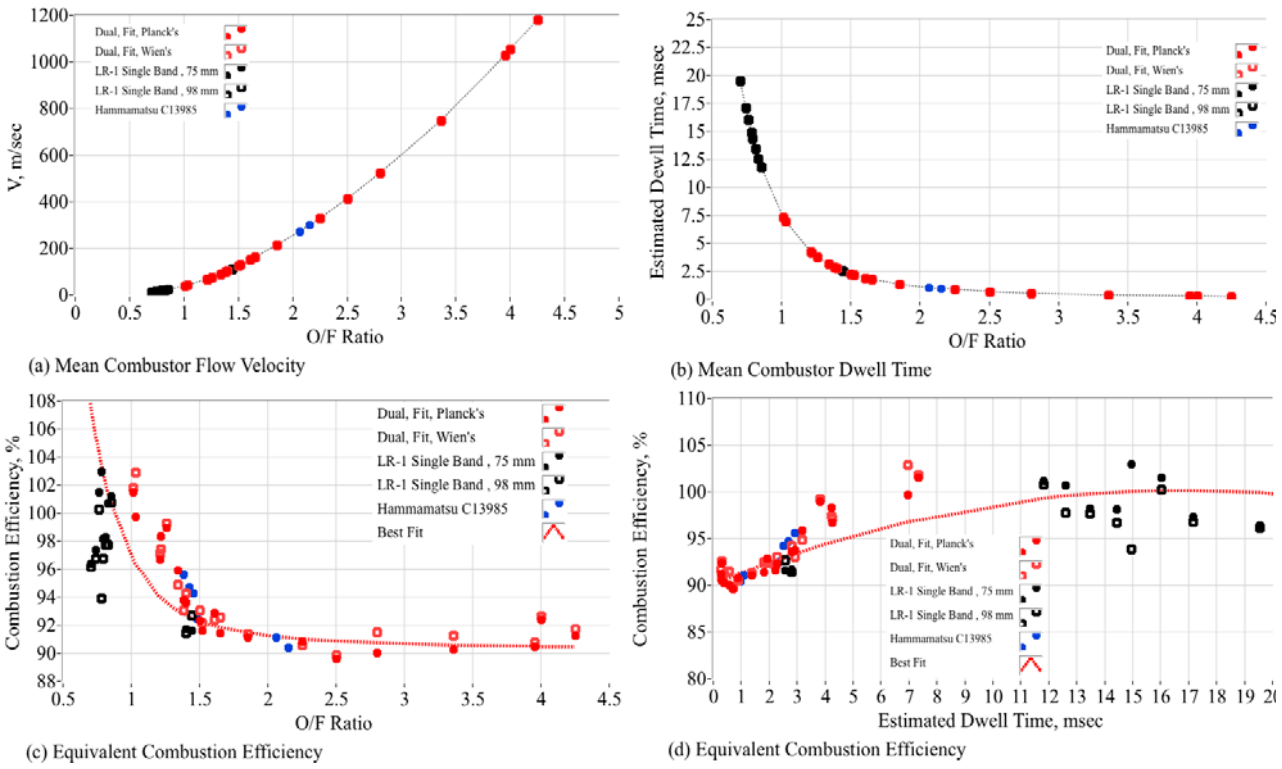

Figure 38. Correlation of η^* with O/F ratio and combustor dwell time.

5.2.4. Nozzle exit plane optical measurements

To date only a small number of tests have been performed using the dual-band arrangement at the nozzle exit. The majority of qualitative results available for the exit plane measurements are single-band using the LR-1 spectrometer and the Thor Labs blue fiber cable. Figure 39 shows results from typical single-ended spectrum example, where spectra from the combustion chamber and nozzle exit plane are compared. These data were collected from the constant throttle burns 2 and 3 of the regression rate tests as presented in Appendix 1, Figure A1-1.

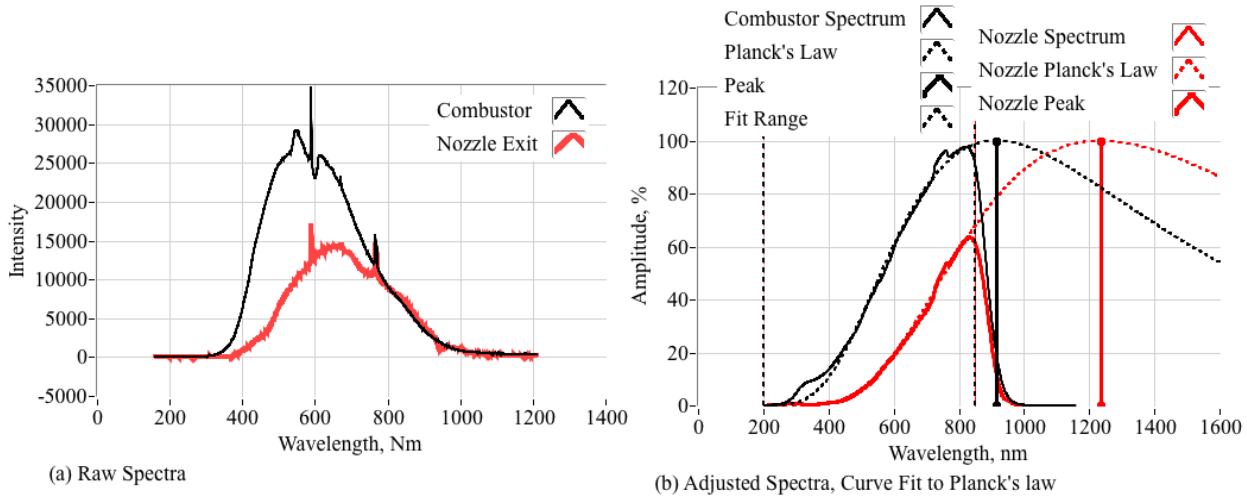

Figure 39. Comparing the combustion chamber and nozzle exit single-ended (visible light) spectra for a constant throttle burn.

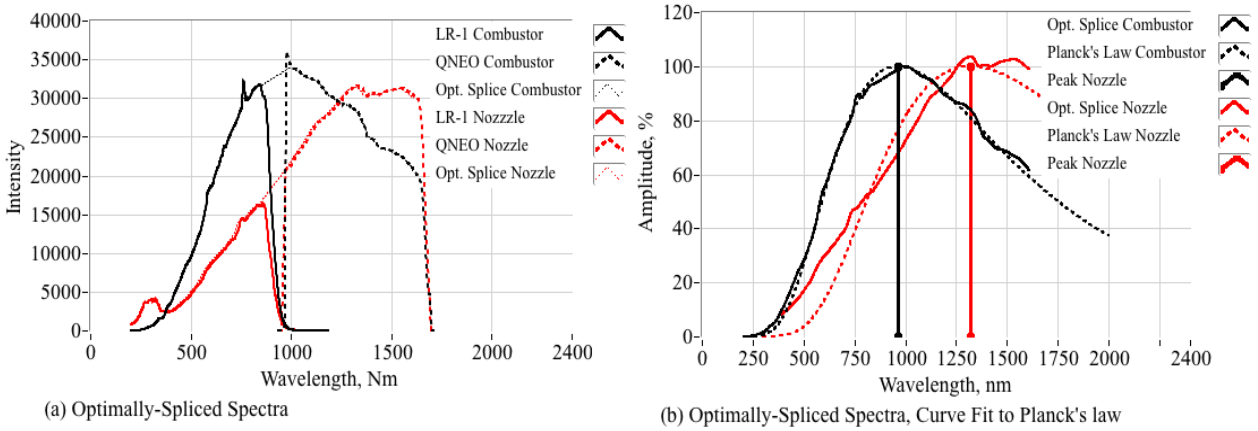

Figure 40. Comparing the combustion chamber and nozzle exit single-ended (visible light) spectra for a constant throttle burn.

Note from Figure 39(a) the nozzle exit optical-intensity exhibits a significantly lower magnitude as well as a distinct "red-shift," indicating a lower flame temperature. Since the valid single-ended data terminate at or round 850 nm, for the nozzle exit spectrum, the extrapolation out to the peak wavelength predicted by Planck's law is significant. The corresponding combustor temperature from the plotted curve fit peak (black-line) is 3008.3 K (2735.1 ℃). The nozzle exit temperature from the plotted curve fit peak (red-line) is 2142.7 K (1869.5 ℃). At the mean O/F ratio of 1.72 for this burn, the corresponding CEA combustor and nozzle exit temperature (from the De Laval analysis) are 3046.5 K (2773.1 ℃) and 2178.7 K (1905.5℃) Thus, even with the significant extrapolation required for the nozzle exit, the temperature difference is less than 50 ℃.

Figure 40 presents a similar comparison, but using the dual-band measurements. Here the corresponding flame temperatures, calculated from the Planck's Law curve-fit are 2990.4 K (2717.3 ℃) for the combustor and 2182.8 K (1909.7 ℃) for the nozzle exit. At the mean O/F ratio of 1.60 for this burn, the corresponding CEA combustor and nozzle exit temperature (from the De Laval analysis)

are 3035.1 K (2763.1 ℃) and 2173.2 K (1900.2 ℃). The higher temperatures of Figure 39 as compared to Figure 40 are likely due to both the single-ended temperature bias, and the slightly higher O/F ratio.

5.2.5. Time-resolved temperature measurements using optical-sensing

The examples as previously presented in the previous sections show only time-averaged temperature properties. However, preliminary analysis has also demonstrated that is may be possible to use the developed fiber-optic techniques to sense time resolved temperature measurements. Data presented by Figure 41 illustrate this capability. Figure 41(a) compares the combustor flame temperature time-history, calculated using the 1-sided LR-1 visible light sensor data against the flame temperature calculated from the CEA data tables using previously-described De Laval flow analysis. Also plotted are (a) motor thrust, (b) O/F ratio, and (c) massflow rates.

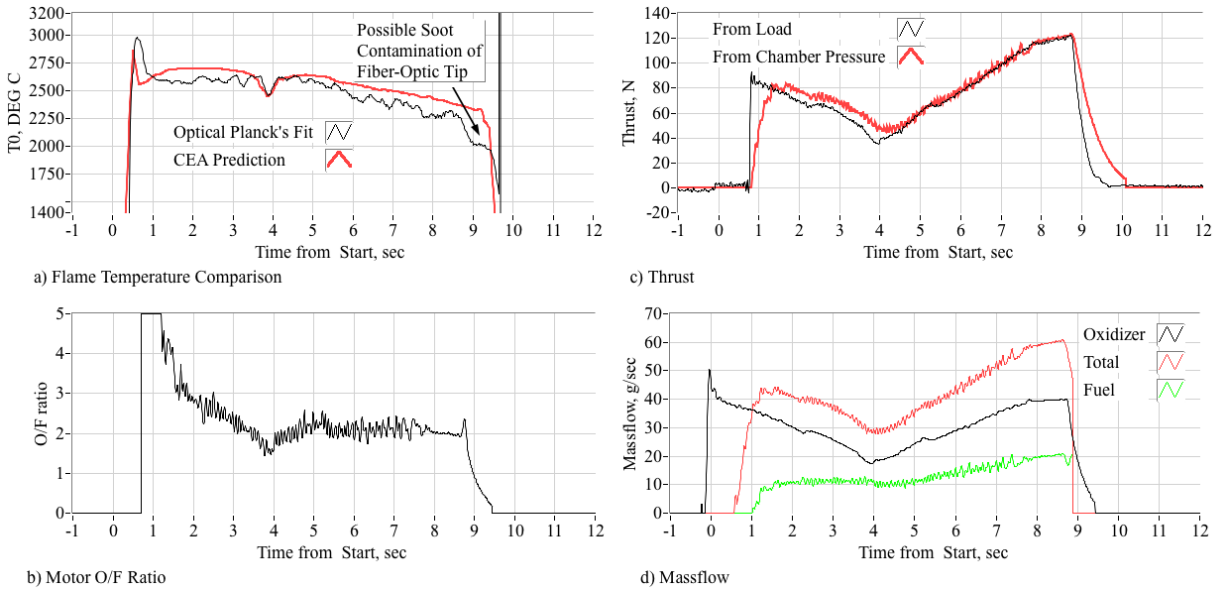

Figure 41. Example of time-resolved optical temperature tracking of combustor flame temperature.

Note, the 1-sided LR-1 flame temperature generally tracks the CEA-derived flame temperature well, both the *qualitatively* and *quantitatively* for the majority of the time history trace; but also exhibits a drop-off of approximately 50–100 ℃ near the latter part of the burn. For this example, the motor is deep throttled and the performance data clearly exhibit a strong fuel-rich O/F shift. Thus, observed temperature drop-off is likely due to soot contamination of the fiber-optic tip. Due to the low response rate of the QNEO spectrometer an equivalent duel-band cannot be performed. While the presented data exhibit good qualitative results, a single example does not prove the case, and considerable work need to be performed in order to verify the time-resolved fidelity and accuracy of the optically-sensed flame temperatures.

5.2.6. Identifying the combustion plume chemical species

For the presented examples of the previous section, the narrow-band emission peaks due to exhaust plume species were “notched” before curve-fitting in order to generate more black-body like

optical signatures. However as exhibited by the raw spectra of Figures 26, 39 and 40, multiple narrow-band harmonics are clearly visible. These peaks correspond to the persistent emission lines released by the ABS fuel during combustion, and any residual oxygen due to the oxidizer flow. The narrow-band emission peaks are most clearly visible in the nozzle exit plume data, where the optical-intensity is significantly reduced.

Figure 42 presents a typical example. Here Figure 42(a),(b) show the visible-light (LR-1) spectra, and Figure 42(c),(d) show the IR (QNEO) spectra. For the visible-light data the strong emission peaks correspond to molecular nitrogen N_2 (570, 744, 746 nm) and atomic oxygen O (558, 630 nm). Two less distinct lower-wavelength emission-lines, likely corresponding to the Balmer [47] series of atomic hydrogen H (364.6 and 397 nm), are also present. The very weak mode at 530 nm, may indicate the presence of carbon (soot) in the plume. The IR (QNEO) spectra exhibit a "valley" that likely corresponds to the absorption line for water at 1380 nm.

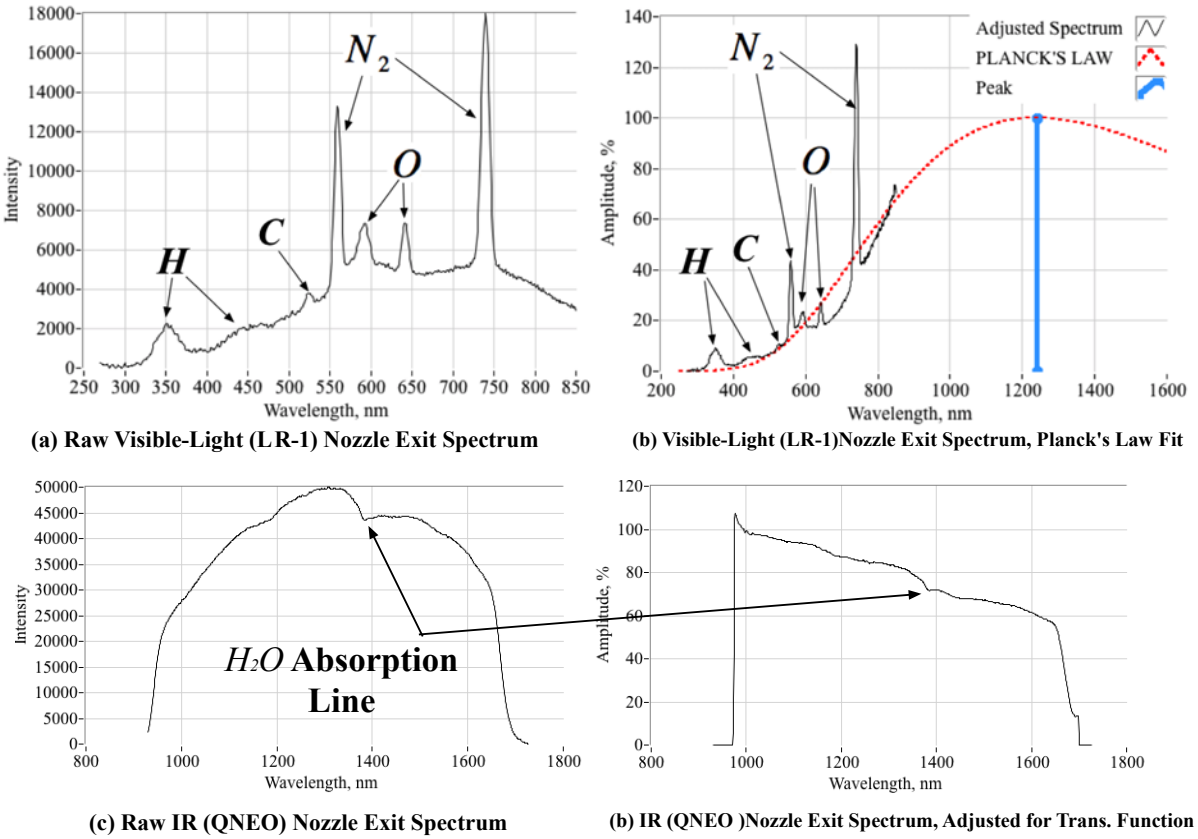

(a) Raw Visible-Light (LR-1) Nozzle Exit Spectrum

(b) Visible-Light (LR-1)Nozzle Exit Spectrum, Planck's Law Fit

(c) Raw IR (QNEO) Nozzle Exit Spectrum

(b) IR (QNEO)Nozzle Exit Spectrum, Adjusted for Trans. Function

Figure 42. Observed emission lines in exit plume visible-light spectrum.

6. Discussion of results

The presented fiber-optic sensing systems performs a function that is analogous to Raman spectroscopy. For the combustion chamber measurements, the dual-band system allows non-contact, high-temperature measurement, and does not interfere with the heat transfer processes. Within the combustion chamber, heat transfer from the flame zone to the fuel wall is offset by the released enthalpy of fusion from the ablating surface (Ref [46]). Also, the internal flow Mach numbers are small,

typically Mach 0.1 to 0.3, and the flow kinetic energy is orders-of-magnitude smaller than the energy of combustion. Even when the fiber-tip protrudes beyond the thermal boundary layer, due to the low flow velocities little kinetic energy is released. Thus, since there is minimal net energy flux across the fuel surface boundary, the internal chamber optical measurements are unlikely to get "confused." While, the curve-fit standard error, approximately 85 ℃, from Figure 37, does not establish the absolute measurement error of the system, it does establish the precision and repeatability of the optical-measurements. Establishing the absolute accuracy of the measurements, using optical tomography such as the methods of Wei et al. [48] or the Raman spectroscopy non-contact methods of Thapa et al. [49] is a prime objective of proposed future work.

As presented by and the supporting analysis, it can be reasoned that the observed drop-off of the optically-sensed flame temperature is a physical occurrence and not an optical-systems measurement error. This drop-off is very likely caused by the reduced combustor dwell time. At the reduced dwell times the plume products do not have sufficient time for complete combustion to occur. This event is analogous to classical characteristic-length L^* combustion inefficiencies as observed in bi-propellant rocket systems [50].

The data as presented Figures 39 and 40 are promising, and the presented data clearly show that the fiber-optic systems can also be used to sense gas temperatures across a solid, non-receding boundary. The exhibited behaviors for the nozzle exit temperatures are certainly qualitatively correct. It must be noted, however, that the repeatability and fidelity of the optically-sensed nozzle exit data are less certain than for the internal combustion chamber measurements.

Clearly, a net energy-flux balance is not experienced at the nozzle exit plane. Ad hoc experimentation with a few of the test runs has shown that the optically-sensed gas temperature at the nozzle exit lane is very-sensitive to the fiber-optic positon in the flow field. Exit plane Mach numbers are typically high, greater than Mach 3.0, and when the fiber is inserted too far into the flow-field a local stagnation region is generated. This flow stagnation kinetic energy, and results in a higher-than expected flame temperature. Similarly, when the fiber burns back entirely to the nozzle wall, heat absorption by the solid-boundary tends to make the optical temperature reading lower-than expected. These energy-transfer effects have yet to be quantified and calibrated. Considerable work must still be performed in order to assess the quantitative accuracy of the nozzle exit temperature measurements.

Even with this limitation, the demonstrated qualitative accuracy of the exit-plane temperature measurements is important. As more dual-band data become available, it is expected that the accuracy of the exit plan temperature measurement will be established. Although the original objectives of this fiber-optic system were intended to sense internal combustor flame temperatures where the fuel boundary recedes, the presented data makes clear that the approach works equally when the fiber optic protrudes from a solid boundary into the flow field. This result opens up the possibility for the presented fiber-optic techniques to be applied for a wide swath of gas-generators, including gas turbine engines.

Finally, analysis of the plume-exit data clearly identifies a suite of species known to be present in the exhaust plume. These results are very promising for future combustion applications. However, while the data of Figure 42 are at least qualitatively correct, insufficient data exists at this point to apply the Beer-Lambert Law [51] in order to perform quantitative to determine the molar concentrations of these species. In order to perform this analysis; a more comprehensive set of tests are required. For future work, it is proposed to fabricate fuel grain sections from 3-D printing feedstock blended with elemental additives such as copper, iron, graphite, or aluminum. These additives will have precisely known emission lines and relative mass concentrations. With these known spectral

emission lines the additive materials would provide very precise benchmarks. Previously, ABS feed stock has been infused with copper powders with relative weights of 2, 4, and 6%. Whitmore et al. [52] report this result. Thus, the proposed this infusion methodology is well-established, and infusion procedures are readily-available.

7. Conclusions

The propulsion research lab at Utah State University has developed a minimally-intrusive optical sensing system for high-temperature/high-velocity gas-generator exhaust plumes. For this application glass fiber-optic cables, acting as radiation conduits, are inserted through the combustion chamber or nozzle wall and look directly into the flow core. The cable transmits data from the flame zone to externally-mounted spectrometers. In order to capture the full-optical spectrum, a blended dual-spectrum system was employed, with one spectrometer system tuned for best-response across the visible-light and near-infrared spectrum, and one spectrometer tuned for best-response in the near- and mid-infrared spectrum. The dual-band sensors are radiometrically-calibrated and the sensed-spectra are spliced together using an optimal Wiener filtering algorithm to perform the deconvolution. The merged spectrum is subsequently curve-fit to Planck's black-body radiation law, and flame temperature is calculated from associated curve maxima (Wien's law). In this report data collected from a lab-scale hybrid rocket system are analyzed using the described methods. Presented data clearly demonstrate the dual-band in-situ measurement system operates as designed, and with a high level of accuracy. Optically-sensed flame-temperatures are correlated to analytical predictions, and shown to generally agree within a few degrees. Additionally, local maxima in the optical spectra are shown to correspond to emission wavelengths of atomic hydrogen and oxygen, water vapor, and molecular nitrogen; all species known to exist in the hybrid combustion plume. Presented data demonstrate that selected fiber-optics can survive temperature greater than 3000 ℃, for durations of up to 25 seconds. This study concludes that the optically-sensed flame-temperature agrees with the theoretically-predicted values, observed deviations of the optically-sensed flame temperature estimates from ideal values result from a physical occurrence—reduced combustion efficiency in the motor—and not a systematic optical-systems measurement error. Although the original objectives of this fiber-optic system were intended to sense internal combustor flame temperatures where the fuel boundary recedes, the presented data makes clear that the approach works equally when the fiber optic protrudes from a solid boundary into the flow field. This result opens up the possibility for the presented fiber-optic techniques to be applied for a wide swath of gas-generators, including gas turbine engines.

Use of AI tools declaration

The authors declare they have not used Artificial Intelligence (AI) tools in the creation of this article.

Acknowledgments

We would like to thank the NASA Marshall Space Flight Center for Funding this work through Cooperative Agreement 80NSSC22M0232. *"In-Situ Optical Measurements of Solid and Hybrid-Propellant Combustion Plumes."*

Conflict of interest

The authors declare there is no conflict of interest.

References

1. R. Gardon, An instrument for the direct measurement of intense thermal radiation, *Rev. Sci. Instrum*., **24** (1954), 366–370. https://doi.org/10.1063/1.1770712
2. S. A. Whitmore, C. I. Frischkorn, S. J. Peterson, In-situ optical measurements of a GOX/ABS hybrid rocket plume**,** in *AIAA SciTech Forum*, 2022. https://doi.org/10.2514/6.2022-0771.
3. S. A. Whitmore, C. I. Frischkorn, S. J. Petersen, In-situ optical measurements of solid and hybrid-propellant combustion plumes, *Aerospace*, **9** (2022), 57. https://doi.org/10.3390/aerospace9020057
4. *1000ft Aqua Plenum Zipcord Duplex Fiber-Optic Cable, 50/125*, Cable Wholesale. Available from: https://www.cablewholesale.com/specs/11f1-301nh.php.
5. *MS Series Mini-Spectrometers*, Hamamatsu. Available from: https://www.hamamatsu.com/resources/pdf/ssd/c10988ma-01_etc_kacc1169e.pdf.
6. *Standard Reference Database Number 69*, National Institute for Standards in Technology (NIST). Available from: http://webbook.nist.gov/chemistry.
7. K. Othmer, *Encyclopedia of Chemical Technology*, John Wiley & Sons, New York, 2006. https://doi.org/10.1002/0471238961
8. Styrene, *National Library of Medicine, PubChem*, Available from: https://pubchem.ncbi.nlm.nih.gov/compound/Styrene.
9. S. Gordon, B. J. McBride, *Computer Program for Calculation of Complex Chemical Equilibrium Compositions and Applications*, NASA, 1994.
10. R. C. Dougal, The presentation of the Planck radiation formula (Tutorial), *Phys. Educ.*, **11** (1976), 438–443. https://doi.org/10.1088/0031-9120/11/6/008
11. J. Walker, *Fundamentals of Physics*, 12th edition, John Wiley, (2021), 891–892.
12. *The HITRAN Database*, Atomic and Molecular Physics Division, Harvard-Smithsonian Center for Astrophysics. Available from: https://lweb.cfa.harvard.edu/hitran/.
13. J. Bertie, *Spectra*, John Bertie's Download Site. Available from: https://sites.ualberta.ca/~jbertie/JBDownload.HTM - Spectra.
14. *Water Absorption Spectrum*. Available from: https://www.idc-online.com/technical_references/pdfs/chemical_engineering/Water_absorption_spectrum.pdf.
15. W. F. Meggers, C. H. Corliss, B. F. Scribner, *Tables of Spectral-Line Intensities, Arranged by Elements*, 2nd edition, National Bureau of Standards, **145** (1974).
16. *Basic Atomic Spectra, Persistent Lines of Neutral Nitrogen (NI)*, NIST. Available from: https://physics.nist.gov/PhysRefData/Handbook/Tables/nitrogentable3.htm.
17. *Basic Atomic Spectra, Persistent Lines of Neutral Hydrogen (NH)*, NIST. Available from: https://physics.nist.gov/PhysRefData/Handbook/Tables/hydrogentable3.htm.
18. *Basic Atomic Spectra, Persistent Lines of Neutral Oxygen (NO)*, NIST. Available from: https://physics.nist.gov/PhysRefData/Handbook/Tables/oxygebtable3.htm.

19. F. Ottonello-Briano, C. Errando-Herran, H. Rödjegård, H. Martin, H. Sohlström, B. Kristinn, et al., Carbon dioxide absorption spectroscopy with a mid-infrared silicon photonic waveguide, *Opt. Lett.*, **45** (2020), 109–112. https://doi.org/10.1364/OL.45.000109
20. *Pro-X, A Better Way to Fly, Pro75® hardware*, Cesaroni. Available from: http://pro75.com/products/pro75/pro75.php.
21. *Impact-Resistant Easy-to-Form ABS Rods*, McMaster-Carr. Available from: https://www.mcmaster.com/abs/shape~rod-and-disc/.
22. S. A. Whitmore, N. Inkley, D. P. Merkley, Restartable Ignition Devices, Systems, and Methods Thereof, USA Patent No. 2015032289A1, 2015. Available from: https://patents.google.com/patent/US20150322892A1/en. (Accessed on 15 November, 2023).
23. *ULTRAVOLT C Series High Voltage CAP-Charging Supplies*, Advanced Energy. Available from: https://www.advancedenergy.com/globalassets/resources-root/data-sheets/ultravolt-c-series-data-sheet.pdf. (Accessed on 15 November, 2023).
24. *1/4 in. Compact Electric Actuated Brass Ball Valve 24 VDC*, Valworx. Available from: https://www.valworx.com/product/compact-electric-actuated-lead-free-brass-ball-valve-14-24-vdc/electric-actuated-brass-ball-valves-compact.
25. *Hamamatsu Mini-Spectrometers [Micro Series] C12880MA, C16767MA*, 2021. Available from: https://www.hamamatsu.com/content/dam/hamamatsu-photonics/sites/documents/99_SALES_LIBRARY/ssd/c12880ma_c16767ma_kacc1226e.pdf.
26. *SMA-905 Specialty Fiber Optic Components and Solutions for Advanced Applications*, Kientec. Available from: https://www.kientec.com/products/connectors/sma-905-connector/.
27. *Fixed Fiber Optic Attenuators, Multimode*, Thor Labs. Available from: https://www.thorlabs.com/newgrouppage9.cfm?objectgroup_id=10463.
28. *LR1-Compact Spectrometer, User's Guide*, Available from: https://www.aseq-instruments.com/LR_spec_full.pdf.
29. *AFBR-S20N1N256, QNEO*, Broadcom. Available from: https://www.broadcom.com/products/optical-sensors/spectrometers/spectrometers-qneo/afbr-s20n1n256.
30. *Fiber-Optic Cable Tutorial*, ARC Electronics, 2007. Available from: https://www.arcelect.com/fibercable.htm.
31. *Single-Mode Optic Fiber*, Wikipedia, Available from: https://en.wikipedia.org/wiki/Single-mode_optical_fiber.
32. *Multi-mode Optical Fibers*, Newport. Available from: https://www.newport.com/c/multi-mode-optical-fibers.
33. FOA, *Guide to Fiber-optics and Premised Cabling, Plastic Optical Fiber (POF)*. Available from: https://www.thefoa.org/tech/pof.htm.
34. *Fiber Optic Basics*, Newport. Available from: https://www.newport.com/t/fiber-optic-basics.
35. *F-MBC Newport Multimode Fiber*, Newport. Available from: https://www.newport.com/p/F-MBC.
36. *FT600UMT Multimode Optical Fiber, High OH for 300–1200 Nm, TECS Clad*, Thor Labs. Available from: https://www.thorlabs.com/thorproduct.cfm?partnumber=FT600UMT.
37. *Fixed Fiber Optic Attenuators, Multimode*, Thor Labs. Available from: https://www.thorlabs.com/newgrouppage9.cfm?objectgroup_id=10463.

38. M. P. Teillet, Image correction for radiometric effects in remote sensing, *Int. J. Remote Sens.*, **7** (1986), 1637–1651. https://doi.org/10.1080/01431168608948958
39. *Compact Stabilized Broadband Light Sources*, Thor Labs. Available from: https://www.thorlabs.us/newgrouppage9.cfm?objectgroup_id=7269.
40. *Bandpass Filter Kits*, Thor Labs. Available from: https://www.thorlabs.com/newgrouppage9.cfm?objectgroup_id=873.
41. S. A. Whitmore, A variational method for estimating time-resolved hybrid fuel regression rates from chamber pressure, in *AIAA Propulsion and Energy 2020 Forum*, 2020. https://doi.org/10.2514/6.2020-3762
42. J. D. Anderson, *Modern Compressible Flow*, 3rd Edition, New York, McGraw Hill, (2003), 127–187.
43. J. S. Meditch, E. C. Tacker, Stochastic optimal linear estimation and control, *IEEE Trans. Syst. Man Cybern.*, **2** (1972), 444–448. https://doi.org/10.1109/TSMC.1972.4309146
44. R. K. Otnes, L. Enochson, *Applied Time Series Analysis*, Wiley, New York, (1978), 219–260. https://doi.org/10.1121/1.383336
45. G. Zilliac, M. Karabeyoglu, Hybrid rocket fuel regression rate data and modeling, in *AIAA Joint Propulsion Conference*, 2006. https://doi.org/10.2514/6.2006-4504
46. S. A. Whitmore, S. L. Merkley, Radiation heating effects on oxidizer-to-fuel ratio of additively manufactured hybrid rocket fuels, *J. Propul. Power*, **35** (2019), 863–878. https://doi.org/10.2514/1.B37037
47. J. J. Balmer, Note on the spectral lines of hydrogen, *Ann. Phys.*, **261** (1885), 80–87. https://doi.org/10.1002/andp.18852610506
48. H. Wei, D. I. Pineda, C. S. Goldenstein, R. M. Spearrin, Tomographic laser absorption imaging of combustion species and temperature in the mid-wave infrared, *Opt. Express*, **26** (2018), 20944–20951. https://doi.org/10.1364/OE.26.020944
49. J. Thapa, M. P. Buric, B. T. Chorpening, *Non-Contact High-Temperature Measurement Using Raman Spectroscopy*, US Department of Energy, National Energy Technology Laboratory. Available from: https://netl.doe.gov/sites/default/files/netl-file/2018_Poster-24_Thapa_NETL.pdf.
50. G. P. Sutton, O. Biblarz, *Rocket Propulsion Elements*, 9th edition, Chapter 6, John Wiley & Sons, 2016.
51. *The Beer Lambert Law, Transmittance & Absorbance*, Edinburgh Instruments. Available from: https://www.edinst.com/us/blog/the-beer-lambert-law/.
52. S. A. Whitmore, K. C. Olsen, P. Forster, C. Y. Oztan, V. L. Coverstone, Test and evaluation of copper-enhanced, 3-D printed ABS hybrid rocket fuels, in *AIAA Propulsion and Energy 2021 Forum*, 2021. https://doi.org/10.2514/6.2021-3225

Appendix 1. Fuel pyrolysis/regression rate calibration

The fuel pyrolysis rate is primarily driven by the oxidizer mass flux rate, and when combined with the changing surface area of the burning fuel, sets the O/F ratio response for the motor. Due to interdependence between fuel massflow, oxidizer massflow, and instantaneous O/F ratio, the fuel regression rate of hybrid motors varies non-linearly with time and is somewhat difficult to measure in real time. Various techniques exist to collect time resolved regression measurements, including the study described in Whitmore (2020) (Ref [41]).

For the steady-throttle burns, the depleted fuel and oxidizer masses are used to calculate fuel

regression rate and oxidizer mass flux over the course of the burn using a mass depletion model. This method is tedious but generally accurate for time averaged calculations. The oxidizer and fuel weights are measured pre- and post- test then divided by burn time to calculate mean massflow rate. The time-averaged longitudinal mean regression rate over the burn duration t_{burn}, is calculated from the consumed fuel mass ΔM_f, as in Eq (A1.1).

$$\dot{r}_L = \frac{\Delta M_f / t_b}{2\pi \cdot \rho_f \cdot \left[\frac{r_L(t_b) + r_0}{2}\right] \cdot L} \tag{A1.1}$$

In Eq (A1.1) r_0 is the initial fuel port radius and r_L is the mean measured fuel port radius at the end of the burn time t_b. The instantaneous fuel port radius is estimated by

$$\dot{r}_L = r_0 + \dot{r}_L \cdot t \,. \tag{A1.2}$$

In Eq (A1.2) r_0 is the initial fuel port radius and t is the burn time. In order to measure variation in fuel regression rate over time, a set of 3 steady state burns were performed on one ABS fuel grain, each at 100% throttle, and pre- and post-burn masses were collected.

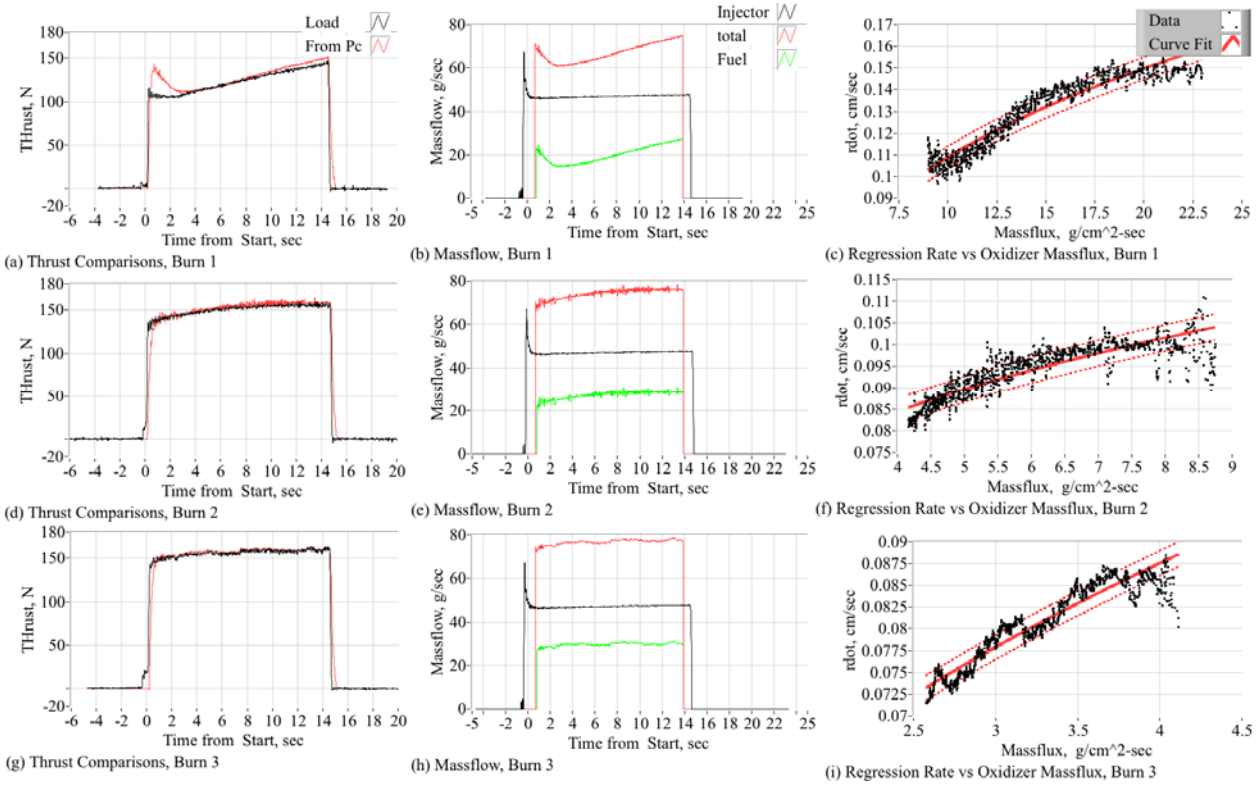

Figure A1-1. Hot fire data from steady state fuel regression burns.

Figure A1-1 the results of three successive constant-throttle regression rate tests performed on a single fuel grain. Figure A1-1(a),(d), and (g) show thrust profile as directly measured by test stand load cell and thrust as calculated from chamber pressure using the De Laval flow equations. Figure A1-1(b),(e), and (h)

plot oxidizer, fuel, and total massflow rates (calculated as previously described). Figure A1-1(c),(f), and (i) plot fuel regression rate as a function of fuel port oxidizer mass flux. The data are curve fit with power law curve fits of the form

$$\dot{r} = a \cdot G_{ox}^{n} \quad . \tag{A1.3}$$

In Eq (A1.3) G_{ox} is the core oxidizer massflux, given by

$$G_{ox} = \frac{\dot{m}_{ox}}{A_{port}} = \frac{\dot{m}_{ox}}{\frac{\pi}{4} D_{port}^{2}} \quad , \tag{A1.4}$$

and $\{a,n\}$ are the curve fit parameters. The associated curve-fit error bands are also plotted. Note that thrust, total massflow, and fuel massflow vary strongly for the first burn, moderately for the second burn, and are relatively steady for the final burn even though the oxidizer massflow rate remains constant for each burn.

Figure A1-2 plots the regression rates from Figure A1-1, overlapped and merged to calculate a cumulative exponential curve fit. Table A1-1 summarizes the curve fit data for both burn series. The curve fit coefficients and associated fit errors for each individual burn, as well as for the concatenated data sets are listed. When averaged over all 6 burns, the resulting curve fit parameters for the mean fuel regression rate are listed in the last column of Table A1-1.

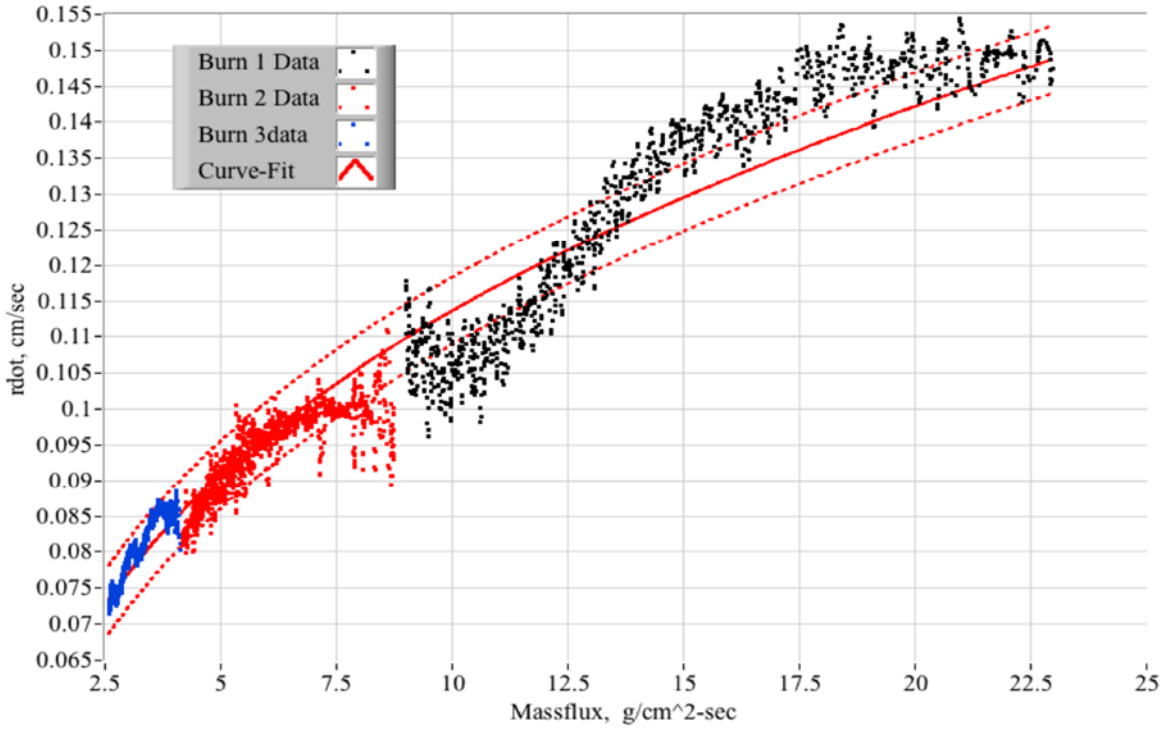

Figure A1-2. Combined fuel regression rates for three 100% throttle burns.

Table A1-1. Test data: Motor fuel regression rate power law curve fit coefficients.

Throttle Level	50%			100%		
Fit Coefficients	a, $\frac{cm/s}{(g/cm^2-s)^n}$	n	RMS Fit Error, *cm/s*	a, $\frac{cm/s}{(g/cm^2-s)^n}$	n	RMS Fit Error, *cm/s*
Burn 1	0.00330	0.2536	±0.0125	0.043	0.2836	±0.0225
Burn 2	0.00405	0.3396	±0.0135	0.0475	0.3796	±0.0155
Burn 3	0.00542	0.4265	±0.0141	0.0625	0.4065	±0.0161
Concatenated Data	0.00414	0.3400	±0.0112	0.0506	0.3239	±0.0121
Mean Values				0.046	0.3320	±0.0117

Reference [45] shows that for a cylindrical fuel port, the hybrid O/F shift and the rate of O/F shift are described by

$$(a)\ O/F = \frac{\dot{m}_{ox}}{m_{fuel}} = \left(\frac{1}{4^n \cdot \pi^{1-n}}\right) \cdot \left(\frac{\dot{m}_{ox}{}^{1-n}}{a \cdot \rho_{fuel}}\right) \cdot \left(\frac{D^{2n-1}}{L^{m+1}}\right)$$

$$(b)\ \frac{\partial\left(O/F_{(t)}\right)}{\partial t} = \frac{\left(2n-1\right)}{2} \cdot \left(\frac{\dot{m}_{ox}}{\rho_{fuel} \cdot \frac{\pi}{4} D^2 \cdot L}\right) = \frac{\left(2n-1\right)}{2} \cdot \left(\frac{\dot{m}_{ox}}{\rho_{fuel} \cdot V}\right). \quad \text{(A1.5)}$$

From Eq (A1.5), as port diameter grows during the fuel burn; for burn exponent ***n > 1/2***, the O/F ratio experiences a positive shift and the motor burns increasingly *leaner with time*. For a burn exponent exactly equal to 1/2, the *burn* is neutral and the motor *experiences no O/F shift* with time. Finally, for burn exponent ***n < 1/2***, the motor burns increasingly *fuel rich with time*, and the O/F shift is negative. The O/F shift comes from a decreasing oxidizer massflux over time, traded-off against an increasing fuel burn area. This behavior has a major influence on the observed motor burn profiles. Assuming a constant oxidizer massflow rate, a positive O/F shift motor will generally see a drop off in thrust as the motor burns, and a negative O/F motor will experience an increase of thrust with time.

Appendix 2. Deriving the relationship between o/f ration and combustor dwell time

Assuming a fuel regression rate model of the exponential form

$$a \cdot G_{ox}^{n}, \quad \text{(A2.1)}$$

and allowing that the fuel massflow rate is given by,

$$\dot{m}_f = A_{burn} \cdot \rho_f \cdot \dot{r}, \quad \text{(A2.2)}$$

the O/F ratio can be written as

$$O/F = \frac{\dot{m}_{ox}}{\dot{m}_f} = \frac{\dot{m}_{ox}}{\left(\pi \cdot D_{port} \cdot L\right) \cdot \rho_f \cdot \left(a \cdot G_{ox}^n\right)} \,. \tag{A2.3}$$

In Eqs (A2.2) and (A2.3) D_{port} and L is the instantaneous fuel port diameter and length, and ρ_f is the fuel mass-density. The burn coefficients $\{a, n\}$ used in Eq (A2.1) are taken from the regression rate analysis as presented in Appendix 1. Substituting for the oxidizer massflux G_{ox},

$$G_{ox} = \frac{\dot{m}_{ox}}{A_{port}} = \frac{\dot{m}_{ox}}{\frac{\pi}{4} D_{port}^2} \,, \tag{A2.4}$$

collecting terms and simplifying,

$$O/F = \frac{\dot{m}_{ox}{}^{1-n} \left(\frac{\pi^{n-1}}{4^n} D_{port}^{2n-1} \right)}{\rho_f \cdot a \cdot L} \,. \tag{A2.5}$$

Solving for the oxidizer massflow,

$$\dot{m}_{ox} = \left(O/F \cdot \left(a \cdot \rho_f \cdot L\right) \cdot \left(\frac{1}{D_{port}} \right)^{2n-1} \cdot \left(\frac{\pi^{n-1}}{4^n} \right) \right)^{\frac{1}{1-n}} \,. \tag{A2.6}$$

Writing the total fuel-port massflow in terms of the O/F ratio,

$$\dot{m}_{tot} = \dot{m}_{ox} + \dot{m}_{fuel} = \frac{O/F+1}{O/F} \dot{m}_{ox} =$$

$$\left(\frac{O/F+1}{O/F} \right) \cdot \left(O/F \cdot \left(a \cdot \rho_f \cdot L\right) \cdot \left(\frac{1}{D_{port}} \right)^{2n-1} \cdot \left(\frac{\pi^{n-1}}{4^n} \right) \right)^{\frac{1}{1-n}} \,. \tag{A2.7}$$

From the equation of continuity (Anderson [42, Chapt. 5]),

$$\dot{m}_{tot} = \rho_{tot} \cdot \frac{\pi}{4} D_{port}^2 \cdot V_{port} = \rho_{ox} \cdot \left(\frac{O/F+1}{O/F} \right) \frac{\pi}{4} D_{port}^2 \cdot V_{port} \,, \tag{A2.8}$$

where V_{port} is the mean fuel port flow velocity. Substituting Eq (A2.8) in (A2.7),

$$\left(\frac{O/F+1}{O/F} \right) \cdot \left(O/F \cdot \left(a \cdot \rho_f \cdot L\right) \cdot \left(\frac{1}{D_{port}} \right)^{2n-1} \cdot \left(\frac{\pi^{n-1}}{4^n} \right) \right)^{\frac{1}{1-n}} =$$

$$\rho_{tot} \cdot \frac{\pi}{4} D_{port}^2 \cdot V_{port} = \rho_{ox} \cdot \left(\frac{O/F+1}{O/F} \right) \frac{\pi}{4} D_{port}^2 \cdot V_{port} \,, \tag{A2.9}$$

and solving for flow velocity,

$$V_{port} = \frac{\left(O/F \cdot \left(a \cdot \rho_f \cdot L \right) \cdot \left(\frac{1}{D_{port}} \right)^{2n-1} \cdot \left(\frac{\pi^{n-1}}{4^n} \right) \right)^{\frac{1}{1-n}}}{\rho_{ox} \cdot \frac{\pi}{4} D_{port}^2} . \tag{A2.10}$$

Finally, the flow combustor dwell time can be written explicitly in terms of *O/F* ratio as

$$\tau_{dwell} = \frac{L}{V_{port}} = \frac{L \cdot \rho_{ox} \cdot \frac{\pi}{4} D_{port}^2}{\left(O/F \cdot \left(a \cdot \rho_f \cdot L \right) \cdot \left(\frac{1}{D_{port}} \right)^{2n-1} \cdot \left(\frac{\pi^{n-1}}{4^n} \right) \right)^{\frac{1}{1-n}}} . \tag{A2.11}$$